1 **Near real-time atmospheric and oceanic science products of Himawari-8/9**

2 **geostationary satellites over the South China Sea**

4 Jian Liu[1], Jingjing Yu[1], Chuyong Lin[1], Min He[1], Haiyan Liu[1], Wei Wang[2], Min Min[2]*

7 [1] School of Geography and Ocean Science, Ministry of Education Key Laboratory for Coast

8 and Island Development, Nanjing University, Nanjing 210023, China, and Southern Marine

9 Science and Engineering Guangdong Laboratory (Zhuhai), Zhuhai 519082, China

10 [2] School of Atmospheric Sciences and Guangdong Province Key Laboratory for Climate

11 Change and Natural Disaster Studies, Sun Yat-sen University, Zhuhai 519082, China

18 *Corresponding author: minm5@mail.sysu.edu.cn

Abstract

The initial release of near real-time (NRT) atmospheric and oceanic science products from Japanese Himawari-8/9 (H8/9) geostationary (GEO) satellites over the South China Sea (SCS) was unveiled in 2024. The primary objective behind crafting these NRT H8/9 satellite products is to facilitate weather and marine environment monitoring, enhance maritime security, and aid ocean navigation, among other purposes. As part of this investigation, a novel NRT data processing system was devised to generate a variety of regional H8/9 GEO satellite science products within a resolution of 10 minutes and a gridded resolution of $0.05° \times 0.05°$ from November 3, 2022 to the present. This algorithm system was built upon the preceding FengYun (FY) geostationary satellite algorithm testbed (FYGAT), which was the prototype of FY-4 GEO meteorological satellite science product operational processing system. These regional H8/9 GEO satellite science products encompass a range of crucial data such as cloud mask, fraction, height, phase, optical and microphysical properties, layered precipitable water, sea surface temperature, etc. We subjected these products to rigorous evaluations against high-quality analogous satellite products and reanalysis data spanning one year in 2023. The validations underscore a strong consistency between the H8/9 GEO satellite atmospheric and oceanic science products over the SCS and the referenced products. Nevertheless, slight discrepancies in these satellite science products were identified, primarily stemming from variations in sensor/dataset characteristics, retrieval algorithms, and geometric conditions. These outcomes demonstrate the suitability of the first edition of NRT atmospheric and oceanic science products of H8/9 satellites over the SCS in supporting the intended quantitative applications. This NRT GEO satellite data record is publicly accessible through the File Transfer Protocol (FTP) provided by the Southern Marine Science and Engineering Guangdong Laboratory (Zhuhai) in China. Free access to the dataset can be found at https://doi.org/10.6084/m9.figshare.25015853 (Liu Jian, 2024).

Keywords: Cloud; Geostationary Satellite; South China Sea; Layered Precipitable Water; Sea surface temperature.

1 Introduction

The South China Sea is located to the south of mainland China and in the western Pacific Ocean. It stands as the largest and deepest sea area in China, with an average depth of 1212 meters and reaching a maximum depth of 5559 meters. Due to its proximity to the equator, the SCS receives a substantial amount of solar radiation, resulting in high local temperatures and humidity. The regional annual average air temperature ranges from 298.15 K to 301.15 K. Even during the coldest months, the average temperatures remain above 293.15 K, while extreme high-temperature events can reach about 306.15 K. The average sea surface temperature (SST) in the SCS is around 299.15 K, and the seasonal variation is not significant. Furthermore, the South China Sea and the Western Pacific serve as abundant sources of water vapor, leading to considerable precipitation in the SCS. Typhoon-related rainfall accounts for about one-third of the total rainfall in the region. On average, the SCS experiences over 1300 mm of rainfall annually, with the majority concentrated in the summer half-year (Wang et al., 2011; Wang et al., 2009; Ding and Liu, 2001).

The SCS region experiences a distinct tropical maritime monsoon climate. Beginning in October each year, winter air currents originating from Siberia and the Mongolian Plateau consistently flow toward the SCS (Martin and Howland, 1982). As a result, from November to March of the following year, the SCS region is dominated by the northeast monsoon. Starting in April, the SCS is influenced by tropical and equatorial ocean air masses, inducing the prevalence of the southwest monsoon from May to September. Additionally, the SCS is often affected by typhoons during the summer and autumn seasons. About 70% of these typhoons originate from the Western Pacific, east of the Philippines, and the vicinity of the Caroline Islands, while the remaining 30% are generated locally in the sea areas near the Xisha and Zhongsha Islands in the SCS (Ding and Liu, 2001; Wang et al., 2020; Niu and Feng, 2021; Jiang et al., 2023).

Due to the lack of ground-based observations over the SCS, satellites, particularly geostationary (GEO) meteorological satellites, have become the most effective means of observing weather patterns, climate, and environmental changes in oceanic regions. For instance, satellite-based rain rate, SST, outgoing longwave radiation (ORL), and convective clouds, etc. are commonly used to identify the summer monsoon, marine heatwave, rainfall, and convection over the SCS (Liu et al., 2014; Xu et al., 2021; Li et al., 2022b; Koseki et al., 2013; Zhou et al., 2024). In recent years, countries across the

91 world, such as China, U.S., Japan, and Korea, have made their own remarkable progress

92 in the development of next-generation geostationary meteorological satellites.

93 Enhanced imaging capabilities in spectral, temporal, and spatial resolutions of the next-

94 generation GEO meteorological satellite allows for more detailed and accurate

95 observations of cloud formations, atmospheric conditions, and natural disasters like

96 hurricanes and typhoons, such as Fengyun-4A/B (FY-4) operated by the China

97 Meteorological Administration (CMA) and Himawari-8/9 (H8/9) satellites operated by

98 the Japan Meteorological Agency (JMA) (Yang et al., 2017; Schmit et al., 2017; Husi

99 et al., 2019; Kim et al., 2021). In additional to GEO advanced imager, many nations

100 have equipped their geostationary lightning and infrared hyperspectral sounding

101 detection sensors to track and analyze thunderstorms, lightning activities, atmospheric

102 temperature and humidity profiles, and even wind fields in real-time (Min et al., 2017b;

103 Ma et al., 2021; Li et al., 2022a).

104 Although the JAXA (Japan Aerospace Exploration Agency) official FTP site

105 (ftp.ptree.jaxa.jp) has already offered the freely download links for some H8/9 Level-2

106 (L2) science products, such as cloud phase and optical depth (Husi et al., 2019), from

107 July 7 of 2015, to the present with approximate two hours lag, the relatively low

108 timeliness and lack of variety of operational satellite science products have seriously

109 affected the data quantitative applications in weather and marine environment

110 monitoring over the SCS. Particularly, time-delayed GEO satellite products cannot be

111 utilized in maritime security and navigation fields, which are of vital importance as it

112 ensures the safety of crew members, transportation of goods, protection of the marine

113 environment, etc. (Soldi et al., 2021). However, as recommended by the JMA, the near

114 real-time down-sampling full-disk H8/9 Level-1B (L1B) radiance data (including 14

115 bands with horizontal resolutions of 1 km (visible, VIS) and 4 km (near infrared and

116 infrared, NIR and IR bands), and excluding two VIS bands at 0.47 μm and 0.51 μm)

117 are able to be received by using the compact and exclusive geostationary satellite data

118 receiving antenna from the JMA Himawari-Cast (Xia et al., 2023; Wang et al., 2019).

119 Therefore, based on the received real-time H8/9 full-disk L1B data, the primary goal of

120 this investigation is to develop several NRT L2 Atmospheric aNd Oceanic science

121 products over the SCS (abbreviated as NANO_SCS) that are released online. It is the

122 first edition of the NRT H8/9 GEO satellite science products generated by the

123 NANO_SCS system. The next sections will be devoted to the introduction and

124 validation of these NRT H8/9 GEO satellite scientific products. Both the NANO_SCS

satellite data processing and management systems are operated by the Southern Marine Science and Engineering Guangdong Laboratory (Zhuhai) of China.

The subsequent sections of this study are meticulously organized as follows. Section 2 briefly introduces the Himawari-8/9 satellites, elucidating the intricate details of the main processing or production flow, as well as shedding light on the remarkable NRT science products specifically tailored for the South China Sea region. Section 3 shows some sample results and verification of key science products in terms of accuracy and reliability. Section 4 elucidates data download method. Finally, in Section 5, we summarize the main conclusions of this study, while also outlining our future vision plans for further enhancing and expanding the scope of the NANO_SCS dataset.

2 Data production

2.1 Data

The Himawari-8/9 satellites, which are the new-generation and state-of-the-art GEO meteorological satellites operated by the JMA, were successfully launched on October 7, 2014, and November 2, 2016, respectively. These advanced satellites operate in a highly sophisticated three-axis stabilized mode, ensuring high spatial-temporal, precise and stable observations. It is worth highlighting that on December 13, 2022, at 05:00 UTC, the H9 GEO meteorological satellite seamlessly replaced its predecessor, the H8 GEO satellite, marking a significant milestone in GEO satellite operations (https://www.data.jma.go.jp/mscweb/en/index.html). This strategic location allows for comprehensive full-disk observation mode, enabling the satellites to capture detailed imagery of the entire Earth's disk, with a particular focus on the Japanese island and its surrounding areas. The Advanced Himawari Imager (AHI), as a unique and highly advanced optical sensor designed specifically for earth viewing, has 16 independent earth-view bands, covering an extensive range of wavelengths from 0.45 to 13.3 μm. These bands include three visible (VIS) bands, three near-infrared (NIR) bands, and ten infrared (IR) bands, each serving a specific purpose in capturing and analyzing various aspects of the Earth's atmosphere and surface. The AHI routinely operates in two observation modes: a full-disk observation mode that captures full disk images within a 10-minute time interval, and a fast regional scanning mode that allows for swift maneuvering and scanning within a 2.5-minute interval. This regional scanning mode is particularly useful for capturing high-resolution imagery of specific regions of

158   interest, enabling detailed analysis and examination of localized weather events. The

159   nominal spatial resolutions of the H8/9-AHI sensor vary depending on the specific band

160   being utilized. For the VIS band at 0.65 μm, the spatial resolution is 0.5 km. The NIR

161   bands have a spatial resolution of 1 km, while the IR bands have a spatial resolution of

162   2 km (Husi et al., 2019; Bessho et al., 2016; Letu et al., 2020; Min et al., 2019). In this

163   study, we only used the down-sampling H8/9 L1B radiance data mentioned before to

164   produce NRT dataset. The spatial resolution for the down-sampling VIS band at 0.65

165   μm was reduced to 1.0 km, while the other bands were down-sampled to 4.0 km. The

166   scope of this investigation covers the South China Sea region, specifically from 0° to

167   40°N latitude and 100°E to 140°E longitude. The utilization of IR bands with a spatial

168   resolution of 4.0 km limits the related L2 satellite science products to the same

169   resolution. Therefore, based on the products with the spatial resolution of 4.0 km, the

170   final regional L2 atmospheric and oceanic science products are analyzed and projected

171   into a user-friendly gridded resolution of 0.05° × 0.05°.

172   The NRT GEO satellite retrieval system (or NANO_SCS system) developed in this

173   study also utilizes the high-resolution operational numerical weather prediction (NWP)

174   data from Global Forecast System (GFS) as ancillary data, which has a gridded

175   horizontal resolution of 0.25° × 0.25° and encompasses a 41 vertical layers ranging

176   from 1000 to 0.01 hPa within a 3-hour time interval. The GFS NWP data can be

177   effortlessly accessed and downloaded from the National Oceanic and Atmospheric

178   Administration   (NOAA)   website

179   (https://nomads.ncep.noaa.gov/pub/data/nccf/com/gfs/prod) at four distinct initial

180   forecast times (00_00, 06_00, 12_00, and 18_00 UTC). To ensure optimal efficiency

181   for the operations of subsequent day, only 9 continuous data (ranging from 018, 021,

182   024, ... to 042) generated at a fixed initial forecast time of UTC 06_00 are selectively

183   downloaded within a predefined time period each day (Whitaker et al., 2008).

184   We collect and use one year (2023) of Climate Data Records (CDR) from the latest

185   MODIS (Moderate Resolution Imaging Spectroradiometer) Collection-6.1 Level-2

186   cloud, land surface temperature (LST), and sea surface temperature (SST) products to

187   validate the NRT H8/9 GEO satellite science products (Platnick et al., 2003; Platnick

188   et al., 2017). MODIS, as a key optical sensor aboard NASA's Terra and Aqua polar-

189   orbiting satellites since 1999 and 2002 (respectively), can provide high resolution (1.0

190   km) L2 science products about the Earth's surface and atmosphere

191   (https://search.earthdata.nasa.gov/search). MODIS data are freely available to the

192   public and are widely used by scientists, government agencies, and researchers around

193   the world, which are often used to verify the other congeneric satellite products (Min

194   et al., 2020). Furthermore, we also compare the NRT layered precipitable water (LPW)

195   product over the SCS with matched ERA5 reanalysis data (the fifth-generation

196   European Center for Medium Range Weather Forecasts Reanalysis data). Note that,

197   ERA5 data assimilate infrared radiances and wind data (through atmospheric motion

198   vectors, AMV) from the Himawari satellites (Hersbach et al., 2020). The hourly layered

199   specific humidity data for the same year (2023) with a horizontal resolution of

200    $0.25°×0.25°$ have been downloaded freely from the ERA5 dataset. This data will be

201   employed for the validation of the layered precipitable water product of H8/9 GEO

202   satellite. You can access the data at https://cds.climate.copernicus.eu/cdsapp#!/home.

203

204   *2.2 NRT processing flow and science products*

205   As extensively discussed in the former study by (Min et al., 2017b), significant strides

206   were made in the development of the operational prototypes of FY-4 GEO satellite

207   science product algorithms. These remarkable advancements were achieved through

208   the collaborative efforts of the scientists in the FY-4 GEO satellite Algorithm Working

209   Group (AWG) in China, who successfully developed two highly robust Fengyun

210   science product algorithm testbeds (or FYGAT) specifically tailored for imagers and

211   sounders. For a comprehensive understanding of the intricate details of FYGAT,

212   interested readers are strongly encouraged to refer to the aforementioned literature

213   written by (Min et al., 2017b). The FYGAT for imager is the key module of the

214   NANO_SCS system for rapidly retrieving the first edition of NRT L2 science products

215   of H8/9 GEO satellites.

216   Figure 1 shows the comprehensive NRT processing flowchart of the NANO_SCS

217   system. The dark gray shading cylinder icons in the figure represent the key processing

218   modules of the system, including retrieval, projection, and drawing modules. Following

219   the synthesis of NRT satellite data, the retrieval module initially retrieves the cloud

220   mask product to identify clear and cloudy-sky pixels within the targeted SCS region.

221   Then, for cloudy-sky pixels, he retrieval module sequentially executes algorithms for

222   retrieving cloud fraction, cloud type/phase, cloud top properties, cloud optical and

223   microphysical properties, and cloud base properties products. However. the accurate

224   retrieval of science products from previous algorithms is crucial for the successful

225   execution of subsequent backend algorithms. For instance, the cloud optical and

microphysical properties algorithm relies on inputs such as cloud phase and top properties to determine specific ice/water cloud optical and radiative properties lookup tables (LUT) and atmospheric correction methods above the cloud (Platnick et al., 2017; Walther et al., 2011) used in retrieval procedure. In a stark contrast, other science algorithms for clear-sky pixels can be executed in parallel as they are independent of each other, such as the algorithms for land surface temperature (LST) and sea surface temperature (SST). It is important to note that due to retrieval efficiency and computing resource limitations, the physics-based layered precipitable water (LPW) algorithm (Zhu et al., 2023) is executed only once every half an hour.

Table 1 provides a list of the main NRT H8/9 GEO satellite atmospheric and oceanic science products in the first edition, along with their corresponding variables, generated by the NANO_SCS system from 3 November 2022 to the present. It includes the variable name, valid value, and corresponding notes of satellite science products. These products are stored in the Hierarchical Data Format-5 (HDF5) format within a 10-minute interval. The NRT GEO satellite science product is typically referred to as "AHI9_L2_CLM_20230815_0650_4000M_proj.hdf5". In this naming convention, the abbreviation of "CLM" stands for Cloud Mask (all abbreviations are three characters long), while "20230815_0650" denotes the specific observation time of the satellite data, including year, month, day, hour, and minute. Lastly, "4000M_proj" indicates the spatial resolution of 4000 meters and projected data. Certain related variables, such as cloud top temperature, pressure, and height, are stored in the same HDF5 format GEO satellite science product file, specifically the CTP (Cloud Top Properties) product file (refer to Table 1).

Figure 2 displays the quick view images of cloud top height, cloud mask, cloud base height, and cloud optical depth at 03:00 UTC on July 31, 2023, as well as atmospheric total precipitable water (from LPW product) and SST retrieved at clear-sky pixels at 10:00 UTC on August 15, 2023, over the SCS. These NRT product images are obtained from the NANO_SCS system. The four cloud product subfigures from July 31, 2023, capture the presence of Super Typhoon "Khanun" (its international number: 2306), which originated in the southwestern waters of Guam on July 22, 2023. It has been observed that the cloud system of Super Typhoon "Khanun" can reach maximum cloud top heights exceeding 16 km and minimum cloud base height lower than 1 km. The productions of all the NRT satellite science products and quick view images of the NANO_SCS system are typically delayed by approximately 17 minutes from the

observation time. Besides, a user-friendly quick-view website (http://meteorsatellite.hellosea.org.cn/#/index) has been created to provide users with a convenient way to access and monitor the NRT H8/9 satellite data over the SCS.

3. Results and validations

3.1 Cloud mask and fraction

To differentiate between clear-sky and cloudy pixels in satellite earth-view image, the cloud mask (CLM) product is firstly retrieved by the NANO_SCS system (refer to Figure 1). This serves as a fundamental and primary L2 scientific output of GEO satellite imaging sensors, playing a crucial role in generating high-quality subsequent satellite products. As mentioned in the previous studies (Liang et al., 2023; Wang et al., 2019; Heidinger et al., 2012), we used the new unified cloud mask algorithm (Wang et al., 2019) of early development to retrieve and generate H8/9 CLM product firstly. Utilizing the 0.64, 1.61, 3.88, 7.3, 11.2, and 12.3 μm channels of H8/9-AHI, the CLM algorithm on this GEO satellite will perform 13 distinct cloud/clear-sky tests. These tests are categorized into four groups: solar reflectance (SolRef), infrared (IR), shortwave infrared (SWIR), and spatial uniformity tests (Wang et al., 2019; Xia et al., 2024).

After successfully retrieving the cloud mask product, similar to the MODIS algorithm (Zhao and Girolamo, 2006), cloud fraction (CLF) is calculated in a down-sampled 5×5 neighboring pixel box as follows:

$$Cloud\ Fraction = 100\% \times (A + B)/(5 \times 5), \qquad (1)$$

where A and B represent the total numbers of cloudy and probably cloudy pixels in the same 5×5 neighboring pixel box, respectively. It is noting that the cloud fraction product is also projected into a user-friendly gridded resolution of 0.05° × 0.05°. More descriptions on these two products can be found in Table 1.

A pixel-to-pixel validation was performed on the H8/9 satellite CLM product over the SCS using one year of MODIS data from the NANO_SCS system. To quantitatively assess the quality of the GEO satellite CLM product, we employed four significant scores: the probability of detection (POD) or recall rate, the false-alarm ratio (FAR), the hit rate (HR) or accuracy, and the Kuiper's skill score (KSS). These metrics were divided into PODcld, PODclr, FARcld, and FARclr, indicating clear and cloudy pixels respectively. For detailed equations and meanings, please refer to previous literature (Wang et al., 2019). In Figure 3a~3d, we present two cloud mask comparison samples

294   between H9/AHI GEO satellite and MODIS at 05:10 and 17:20 UTC on January 8,

295   2023. It is evident that the CLM results from H9/AHI align well with the latest MODIS

296   official products across both land and sea. Additionally, Figure 3e displays the POD,

297   FAR, HR, and KSS scores of H9/AHI results for all matched pixels over land and ocean.

298   Notably, both PODcld and HR exceed 0.90, consistent with our prior study (Wang et

299   al., 2019), indicating a relatively high-quality CLM product. Moreover, considering

300   that cloud fraction depends on the cloud mask product (refer to Eq. (1)), we opted

301   against using similar products for verification in this analysis.

302

303   *3.2 Cloud type and phase*

304   Cloud type and phase as thermodynamics characteristics signify the state of water

305   vapor and minuscule particles within the cloud. It plays a critical role in weather and

306   climate research as different cloud phases influence the reflection and absorption of

307   solar radiation, consequently impacting Earth's energy balance and climate change

308   (Mülmenstädt et al., 2021). Due to the similarities in detection channels (using 7.3, 8.5,

309   11.2, and 12.3 μm channels), the cloud type and phase (CLP) retrieval algorithm

310   developed here for H8/9-AHI was based on the corresponding algorithm used for U.S.

311   new-generation Geostationary Operational Environmental Satellites (GOES-R)

312   (Pavolonis et al., 2005; Pavolonis, 2010b). The physical foundation of this algorithm is

313   the radiative transfer equation or forward model for cloudy-sky at a specific infrared

314   wavelength λ, which can be expressed as follows (Min et al., 2020):

315    $I_{obs}(\lambda) = \varepsilon(\lambda)I_{ac}(\lambda) + \varepsilon(\lambda)T_{ac}(\lambda)B(\lambda, t_{eff}) + I_{clr}(\lambda)[1 - \varepsilon(\lambda)],$ (2)

316   where I_{obs} is the observed radiance, I_{clr} is the clear-sky radiance, and I_{ac} is the above-

317   cloud upwelling atmospheric radiance, respectively. I_{clr} can be precisely simulated by

318   the coupled fast IR radiative transfer model in the FYGAT system with the input of

319   matched GFS NWP data. ε and T_{ac} respectively represent the cloud emissivity and

320   above-cloud transmittance. B and t_{eff} are the Planck function and the cloud effective

321   temperature, respectively.

322   From Eq. (2), a pair of effective cloud emissivity from two different channels can be

323   used to calculate the ratio of effective absorption optical thickness τ_{abs} of cloud, which

324   is known as the beta ratio (β) and written as follows (Heidinger and Pavolonis, 2009;

325   Parol et al., 1991):

326    $\beta_{obs} = \frac{\ln[1-\varepsilon(\lambda_1)]}{\ln[1-\varepsilon(\lambda_2)]} = \frac{\tau_{abs}(\lambda_1)}{\tau_{abs}(\lambda_2)},$ (3)

327   Actually, this parameter represents the ratio of the effective absorption optical depth at

328   two different channels or wavelengths. It can describe β_{obs} by utilizing the computed

329   single scattering properties of cloud particles, along with a given cloud particle size

330   distribution and optical properties. (Parol et al., 1991). The β_{theory} can be expressed as

331   follows:

332   $\beta_{theory} = \frac{[1-\omega(\lambda_1)g(\lambda_1)]\alpha_{ext}(\lambda_1)}{[1-\omega(\lambda_2)g(\lambda_2)]\alpha_{ext}(\lambda_2)},$ (4)

333   where ω, g, and α_{ext} are the single scattering albedo, asymmetry parameter, and

334   extinction cross section, respectively. Considering the weak impact of multiple

335   scattering, Parol et al., (1991) demonstrated a good approximation of $\beta_{theory} \approx \beta_{obs}$ in the

336   range of 8~15 μm. Eq. (4) is independent of satellite observed radiance, cloud altitude,

337   or cloud optical thickness. By using β ratio instead of brightness temperature difference

338   (BTD), it not only considers the contribution of clear-sky conditions to radiation but

339   also provides a method to link observations with theoretical cloud particle distribution

340   and optical properties.

341   Based on the differences in β ratios (i.e. β[8.5/11.2μm], β[12.3/11.2μm], and

342   β[7.3/11.2μm]) between ice and water clouds, this algorithm effectively identifies cloud

343   type and phase by integrating cloud emissivity ε with observed brightness temperature.

344   More details of this algorithm can be found from the previous literatures (Pavolonis,

345   2010a; Pavolonis, 2010b). The six specific cloud types of this CLP product include

346   liquid water (cloud top temperature>273K), supercooled water (liquid water clouds

347   with cloud top temperature<273K), mixed (which encompass both ice and water

348   clouds), optically thick ice, optically thin ice, and multilayered ice clouds. The cloud

349   phase product can be defined by summarizing the first three types of clouds and ice

350   phase clouds using the last three different ice clouds (see Table 1).

351   Figure 4 illustrates the cloud phase comparisons between the H9/AHI GEO satellite

352   and MODIS at 05:10 UTC on January 8, 2023, and 04:30 UTC on July 10, 2023. This

353   comparison reveals consistent results between the two products. Notably, in Figures 4a

354   and 4c, the new H9/AHI cloud phase product identifies some newly added mixed-phase

355   cloud targets, a feature lacking in the MODIS official cloud phase product (King et al.,

356   1997). However, despite this addition, the distribution pattern of cloud phases remains

357   consistent between the two products as depicted in Figure 4. The POD and FAR for ice

358   and water clouds (Lai et al., 2019) are 0.94/0.17 and 0.68/0.14, respectively.

359

360   *3.3 Cloud top and base properties*

361   Cloud geometry thickness (CGT), including top and base heights (CTP and CBP),

362   enables the profiling of the vertical structure of clouds, which is vital for understanding

363   global weather and climate systems (Viúdez-Mora et al., 2015; Wang et al., 2022).

364   Using the same beta ratio (β) theory discussed in Section 3.2, the optimal estimation

365   (OE) method (Rodgers, 2000), and observed brightness temperatures (BT) at 11.2, 12.3,

366   and 13.3 μm channels, a classical one-dimensional variational (1DVAR) algorithm

367   applies a cost function ζ (refer to Eq. 5) to estimate the cloud top temperature (CTT),

368   which can be written as follows :

369    $$\zeta = [x - x_a]^T Cov_a^{-1} [x - x_a] + [y - M(x)]^T Cov_y^{-1} [y - M(x)], \qquad (5)$$

370   where x, y, x_a, $M(x)$, Cov_a, and Cov_y, represent the posterior state vectors, the

371   observation vectors (include $BT_{11\mu m}$, $BTD_{11-12\mu m}$, and $BTD_{11-13.3\mu m}$), the priori state or

372   first guessed vectors (include CTT, cloud emissivity ε at 11μm, and β[12/11μm]), the

373   forward radiative transfer model (based on Eq. (2) in the CLP retrieval algorithm), and

374   the error covariance matrices of the priori state vectors (x_a) and the differences between

375   observations and the forward radiative transfer model of $M(x)$, respectively. As a

376   nonlinear least squares fitting problem, the classical Levenberg-Marquardt iteration

377   method is used here to minimize the cost function of ζ, which can be written as follows

378   (Levenberg, 1944):

379    $$\delta x = \left(Cov_a^{-1} + K^T Cov_y^{-1} K\right)^{-1} \left(K^T \left(Cov_y^{-1}[y - M(x)]\right) + Cov_a^{-1}[x_a - x]\right), \qquad (6)$$

380   where K signifies the Jacobi or Kernel matrix. The optimal values of CTT, cloud

381   emissivity, and β[12/11μm] will be obtained when the iteration converges the satellite

382   observation vectors of y. It is worth noting that the beta ratio (β) plays a specific role in

383   this retrieval algorithm by analytically solving equations in the Jacobi matrix stated in

384   Eq. (6), thereby resulting in a significant enhancement of operational processing

385   efficiency. After obtaining the optimal CTT, the matched GFS-NWP temperature

386   profile is utilized to interpolate the corresponding cloud top height and pressure. For

387   more detailed information on the CTP retrieval algorithm of H8/9-AHI, please refer to

388   the study from Min et al., 2020.

389   In contrast, the successful retrieval of cloud base properties requires more inputs such

390   as cloud mask, type, top height, and optical and microphysical properties (convert to

391   cloud water path, CWP, unit = g/m^2) as discussed in Sections 3.1, 3.2, and 3.4. Wang

392   et al. (2023) have recently developed and improved a new CBP retrieval algorithm for

393 GEO H8/9-AHI, which refers to the CLAVR-x cloud base properties algorithm (Clouds

394 from AVHRR Extended, NOAA's operational cloud processing system for the AVHRR)

395 (Wang et al., 2024; Noh et al., 2017). This algorithm can only be executed during the

396 daytime (solar zenith angle < 65°) because it relies on cloud top height (CTH) and cloud

397 water path to calculate the two linear fitting coefficients, namely slope (A_1) and

398 intercept (A_2) (Noh et al., 2017). These two coefficients are determined through

399 piecewise fitting using the CTH, CWP, and cloud base height (CBH) data obtained

400 from the joint CloudSat/CALIPSO (Cloud-Aerosol Lidar and Infrared Pathfinder

401 Satellite Observation) product (Noh et al., 2017). Once the two corresponding fitting

402 coefficients are obtained, the cloud geometric thickness can be calculated as follows:

403 $$CGT = A_1 \times CWP + A_2, \tag{7}$$

404 After that, the CBH can be easily calculated using the formula CBH = CTH − CGT.

405 Previous studies have validated the CTH and CBH products obtained through the

406 same algorithms used for the H8 satellite, leveraging joint CloudSat/CALIPSO product

407 (Wang et al., 2024; Wang et al., 2022; Min et al., 2020; Min et al., 2017b). The mean

408 absolute error (MAE) and standard deviation (STD) for GEO satellite CTH are reported

409 as 3.18 km and 3.75 km, respectively, with a noticeable increase associated with higher

410 CTH values. Additionally, the MAE and root-mean-square error (RMSE) for CBH,

411 retrieved by the same GEO CLAVR-x algorithm, stand at 1.938 km and 2.91 km, as

412 reported in prior studies (Wang et al., 2024; Min et al., 2020). In Figure 5, CTH

413 comparisons between the H9/AHI GEO satellite and MODIS are presented for 18:50

414 UTC on October 8, 2023, and 04:30 UTC on July 10, 2023. The figure well

415 demonstrates consistent CTH values and horizontal distributions derived from both

416 H9/AHI and MODIS datasets.

417

418 *3.4 Cloud optical and microphysical properties*

419 The cloud optical thickness (COT or τ_{cld}) and particle effective radius (CER or r_{cld},

420 unit=μm) (or cloud optical and microphysical properties) primarily characterizes the

421 radiative properties of clouds, highlighting their influence on the equilibrium of Earth's

422 radiation budget (Platnick et al., 2017). These two parameters are commonly used in a

423 general circulation model (GCM) to define cloud parameterization schemes for climate

424 modeling (Chou et al., 1998). The cloud optical and microphysical properties algorithm

425 during the daytime (solar zenith angle < 65°) utilizes the reflected solar radiation

426 measured by a non-absorbing channel (0.64 μm) to retrieve cloud optical thickness (τ_{cld}).

427   Additionally, it uses the reflected solar radiation measured by an absorbing channel

428   (2.23 μm) to retrieve cloud particle effective radius (r_{cld}) (Walther et al., 2011). The

429   fundamental physical principle of this algorithm is to leverage the sensitivities of the

430   non-absorbing and absorbing channels to cloud optical thickness (τ_{cld}) and cloud

431   particle effective radius (r_{cld}) in the atmospheric radiative transfer process, as

432   demonstrated by a previous study (Nakajima and King, 1990).

433   The water and ice cloud optical and radiative properties look-up tables (LUT) with a

434   modified Gamma size distribution for fast retrieval were built based on spherical

435   particle with the scattering properties given by the Mie theory and MODIS Collection-

436   6 severely roughened aggregated columns ice crystal (Min et al., 2017a; Platnick et al.,

437   2017; Baum et al., 2007), respectively. By utilizing the similar 1DVAR algorithm

438   discussed in Section 3.3, along with water/ice cloud LUTs, observed reflectance at 0.64

439   and 2.23 μm channels, and additional ancillary data, the optimal cloud optical thickness

440   (τ_{cld}) and cloud particle effective radius (r_{cld}) can be iteratively calculated using the OE

441   algorithm (Walther et al., 2011). Differing from Equation (2), the variables or first-

442   order partial derivative from forward cloud reflectance model in the Jacobi matrix are

443   derived from a formula for solar reflectance observed by satellite, which can be written

444   as follows (Nakajima and King, 1990):

445     $$R_{obs} = R_{cld} + \frac{A_s}{1 - A_s R'_{cld}} T_{cld} T'_{cld}, \tag{8}$$

446   where R_{obs} is the total cloud bidirectional reflectance function at the top of the

447   atmosphere (TOA). A_s is the albedo at the Lambertian surface of a uniform single-

448   layer cloud. R_{cld} and T_{cld} signify the cloud reflectance and downward transmittance

449   (diffuse and direct), respectively. R'_{cld} and T'_{cld} are the cloud spherical albedo and the

450   transmittance below the cloud, respectively. After retrieving τ_{cld} and r_{cld}, ice and liquid

451   cloud water paths (IWP/LWP) are calculated using empirical formulas (Bennartz, 2007;

452   Heymsfield et al., 2007), which are expressed as follows:

453     $$LWP = \frac{5}{9} \tau_{cld} r_{cld} \rho, \tag{9}$$

454     $$IWP = \frac{\tau_{cld}^{1/0.84}}{0.065}, \tag{10}$$

455   where ρ is the density of liquid water (=1.0 g/cm^3).

456   Figure 6 shows the cloud optical depth and effective radius comparisons between the

457   H9/AHI GEO satellite and MODIS (Platnick et al., 2017) at 05:40 UTC on October 30,

458   2023. We find consistent retrieval results between these two different COT and CER

459   products. Besides, Figures 6e and 6f respectively show the comparisons of the one year

460   COT and CER from MODIS and H9/AHI data over the SCS with the related scores,

461   such as MAE, MBE, R and RMSE. The differences are likely to be attributed to the

462   different spatial resolutions and retrieval algorithms used between these two satellite

463   products (Letu et al., 2019; Wang et al., 2024). Specifically, in Figure 6f, the CER

464   comparisons reveal more pronounced discrepancies, primarily due to the different ice

465   cloud particle scattering models used in the two retrieval algorithms (Letu et al., 2019).

466

467   *3.5 Layered precipitable water and atmospheric instability indices*

468   The atmospheric temperature and humidity profiles provide valuable information

469   about the vertical distribution of water vapor and temperature at various altitudes. This

470   is very crucial for studying cloud formation, precipitation patterns, and the intricate

471   processes of the water cycle, and accurate numerical weather forecasting and climate

472   modeling (Charlesworth et al., 2023; Zheng et al., 2015; Li et al., 2016; Zhu et al.,

473   2023). In this investigation, the layered precipitable water (LPW) product obtained

474   from H8/9-AHI only provides clear-sky (refer to the flowchart in Figure 1) temperature

475   and humidity profiles and atmospheric instability indices. The next few satellite

476   products described in Sections 3.6 and 3.7 will also be processed only in clear-sky

477   pixels. The temperature and humidity profiles will be integrated into three distinct

478   layers for the output satellite product (High layer: from 700 to 300 hPa; Middle layer:

479   from 900 to 700 hPa; Low layer: from the surface to 900 hPa).

480   This physics-based LPW retrieval algorithm uses the BT observations at 6.2, 6.9, 7.3,

481   8.5, 10.4, 11.2, 12.3, and 13.3 μm channels to retrieve temperature and humidity

482   profiles. Since the temperature and humidity profiles can only be retrieved from clear-

483   sky pixels, we can express the forward IR radiative transfer equation observed by

484   satellite sensor as follows (Li et al., 2012; Li et al., 2000):

485    $$I_{obs}(\lambda) = \varepsilon_s(\lambda)B_s(\lambda)T_s(\lambda) - \int_0^{p_s} B(\lambda)dT(\lambda; 0, p) + [1 -$$

486    $$\varepsilon_s(\lambda)] \int_0^{p_s} B(\lambda)dT'(\lambda; 0, p), \qquad (11)$$

487   where T is the atmospheric transmittance above the pressure p. Subscript s signifies the

488   surface, $T' = T_s^2/T$. Similar to the OE method mentioned above, the cost function for

489   retrieving temperature and humidity profiles can be written as follows:

490    $$\zeta = [x - x_a]^T \gamma Cov_a^{-1}[x - x_a] + [y - M(x)]^T Cov_y^{-1}[y - M(x)], \qquad (12)$$

491   where the new added variable γ is the regularization parameter (or smoothing factor)

492   compared to Eq. (5). The introduction of the parameter γ aims to achieve faster

493   convergence and improve solution stability. The iterative 1DVAR algorithm can

494   increase or decrease parameter γ by determining the first-order variation of Eq. (11) (Li

495   et al., 2000). The first guessed temperature and humidity profiles for iterative retrieval

496   are obtained from spatial-temporally matched GFS-NWP data.

497   After retrieving the optimal temperature and humidity profiles, it will calculate five

498   atmospheric instability indices, including LI (Lifted Index), CAPE (Convective

499   Available Potential Energy), TT (Total Totals), KI (K Index), and SI (Showalter Index).

500   In weather forecasting, these indices can characterize the degree of development of

501   atmospheric instability features and provide the forecaster with a general idea of the

502   convective forcing. For instance, the LI represents the level of atmospheric

503   thermodynamic instability. A positive LI value indicates stability ($0<LI$), while a

504   negative LI value suggests varying degrees of instability ($-3< LI <0$ marginally unstable,

505     $-6<LI<-3$ moderately unstable, $-9<LI<-6$ very unstable, and $LI <-9$ extremely unstable)

506   (Fernando et al., 2021). The valid ranges and usages of these five atmospheric

507   instability indices could refer to Table 1 and the study from Li et al., 2012. Note that,

508   considering the specific retrieval efficiency (processing LPW over the SCS region takes

509   approximately 20~25 minutes) of the H8/9-AHI LPW product, we have set the retrieval

510   frequency for LPW to 30 minutes.

511   Figure 7 presents a comparison between the LPW, encompassing total precipitable

512   water and water vapors at low, middle, and high layers, derived from the H9/AHI GEO

513   satellite and ERA5 reanalysis data at 09:00 UTC on January 4, 2023, specifically over

514   the SCS. The right column panel displays associated H9/AHI CAPE, K, LI, and

515   Showalter indices. Except for the water vapors at the high layer (700-300hPa), the

516   remaining LWP products exhibit negligible differences compared to the ERA5

517   reanalysis data in Figure 7.

518   To further validate the LPW products derived from H9/AHI, we conducted

519   comparisons against ERA5 reanalysis data for LPWs over a four-month period

520   mentioned above (January, April, July, and October of 2023). Figure 8 depicts the

521   comparison results for total precipitable water and LPWs at three distinct layers. The

522   correlation coefficients (R) for the LPWs at low, middle, and high layers, along with

523   total precipitable water, are respectively 0.919, 0.784, 0.725, and 0.876. These high

524   correlation coefficients indicate the relatively high quality of this product from the
525   NANO_SCS system.

526

527   *3.6 Land and sea surface temperatures*

528   Land and sea surface temperatures (LST and SST) are essential variables frequently
529   utilized in climate research community (Cai et al., 2022; Hong et al., 2022). In this
530   study, we incorporated a classical land surface temperature algorithm (Ulivieri and
531   Cannizzaro, 1985) into the NANO_SCS system, using split-windows channels of H8/9-
532   AHI (11.2 and 12.3 μm). This modified algorithm was also implemented as the
533   operational LST algorithm for the FY-4A GEO satellite (Dong et al., 2023) in China
534   Meteorological Administration (CMA), which can be easily expressed as follows:

535    $LST = C + A_1 BT_{11\mu m} + A_2(BT_{11\mu m} - BT_{12\mu m}) + A_3\varepsilon_s + D(BT_{11\mu m} -$
536    $\qquad BT_{12\mu m})(sec\theta - 1),$ $\qquad\qquad$ (13)

537   where C, A_{1-3}, and D are the fitting coefficients, respectively. θ represents the satellite
538   zenith angle. ε_s is the surface emissivity. To account for the uncertainties in the LST
539   algorithm caused by water vapor, we conducted regression analysis using MODTRAN
540   V4.2 (Min et al., 2022; Berk et al., 2000; Dong et al., 2023) to derive fitting coefficients
541   for four distinct groups: daytime dry, daytime moist, nighttime dry, and nighttime moist
542   conditions. A threshold of water vapor content = 2.0 g/cm^2 was utilized to classify the
543   atmosphere as either dry or moist. This threshold value was obtained from matched
544   GFS-NWP data.

545   The classical and simplified Non-Linear Sea Surface Temperature (NLSST)
546   algorithm was used here to retrieve SST of H8/9-AHI (Walton et al., 1998), which is
547   expressed as follows:

548    $SST = a_0 + a_1 BT_{11\mu m} + a_2(BT_{11\mu m} - BT_{12\mu m}) + a_3(BT_{11\mu m} -$
549    $\qquad BT_{12\mu m})(sec\theta - 1),$ $\qquad\qquad$ (14)

550   where a_{0-3} are the fitting coefficients. The NOAA latest OISST (optimum interpolation
551   sea surface temperature) are used here to obtain fitting coefficients in Eq. (14) (Huang
552   et al., 2021; Reynolds et al., 2007). This global SST dataset, with a 0.25°×0.25°
553   horizontal resolution, covers the period from 1981 to the present.

554   Figure 9 shows the LST and SST comparisons between H9/AHI GEO satellite and
555   MODIS at 18:40 UTC on October 29, 2023. From this figure, we find consistent results
556   of LST and SST between our results and MODIS official products. Figures 9e and 9f

557 also shows the comparisons of the one year LST and SST from MODIS and H9/AHI

558 data over the SCS. The correlation coefficients (R) of these two products are about 0.96.

559

560 *3.7 Vegetation and water indices*

561   Vegetation and water indices, such as NDVI (Normalized Difference Vegetation

562 Index), NDSI (Normalized Differential Snow Index), NDWI (Normalized Differential

563 Water Index), and LSWI (Land Surface Water Index), are commonly utilized for

564 climate change, vegetation growth, urbanization, flood monitoring, etc. (Zheng et al.,

565 2021; Hall et al., 1995; Xiao et al., 2006; Gu et al., 2007). In the NANO_SCS system,

566 these indices are calculated for clear-sky pixels during daytime using H8/9-AHI and

567 are expressed as follows:

568 $NDVI = (Ref_{0.86\mu m} - Ref_{0.64\mu m}) / (Ref_{0.86\mu m} + Ref_{0.64\mu m}),$ (15)

569 $NDSI = (Ref_{0.64\mu m} - Ref_{1.6\mu m}) / (Ref_{0.64\mu m} + Ref_{1.6\mu m}),$ (16)

570 $NDWI = (Ref_{0.86\mu m} - Ref_{2.23\mu m}) / (Ref_{0.86\mu m} + Ref_{2.23\mu m}),$ (17)

571 $LSWI = (Ref_{0.86\mu m} - Ref_{1.6\mu m}) / (Ref_{0.86\mu m} + Ref_{1.6\mu m}),$ (18)

572 where *Ref* represents the reflectance observed by satellite visible and near infrared

573 bands during the daytime. Unfortunately, in this study, the lack of a 0.47μm channel

574 prevents the computation of the Enhanced Vegetation Index (EVI). Figure 10 shows

575 the clear-sky NDVI, NDSI, NDWI, and LSWI maps from H9/AHI at 04:00 UTC on

576 December 1, 2023 over the SCS, which were generated by the NANO_SCS system.

577

578 **4. Summary**

579   This investigation provides a comprehensive introduction to the key GEO satellite

580 science products generated by the NANO_SCS system and their evaluation. It offers

581 near-real-time atmospheric and oceanic science products of Himawari-8/9

582 geostationary satellites over the South China Sea from November 13, 2022, to the

583 present. Positioned at 140.7°E and 0° latitude, the H8/9 geostationary satellites mainly

584 cover East Asia, Oceania, and the Indian Ocean. The standard NRT Level-2 satellite

585 science products encompass the region between 0° to 40°N latitude and 100°E to 140°E

586 longitude with a grid resolution of 0.05° × 0.05° and a 10-minute interval (except for

587 LPW products, retrieved every 30 minutes). These products are derived from 14

588 spectral channels with a 4km horizontal resolution.

589   The NANO_SCS system provides a range of atmospheric and oceanic products,

590 including cloud mask, fraction, height, phase, optical and microphysical properties,

layered precipitable water, land surface temperature, sea surface temperature, and more. These near-real-time satellite products were rigorously evaluated against independent datasets, including MODIS satellite-based products and ERA5 reanalysis data. The results highlight strong consistency between NRT H8/9 geostationary satellite atmospheric and oceanic science products and the reference data from similar sensors and ERA5 over the South China Sea.

Future continuation of atmospheric and oceanic science products generated by the NANO_SCS system is also operated and secured by the Southern Marine Science and Engineering Guangdong Laboratory (Zhuhai) in China. Preparations are underway for new products such as atmospheric motion vectors (AMV) and quantitative precipitation estimates (QPE) in near-real-time production. Besides, the qualities of current GEO satellite products will be further validated and enhanced. Chinese FY-4C GEO satellite, scheduled for launch in 2025 or 2026, will offer higher spatial resolution and additional channels, including an IR hyperspectral sounder, to further extend and improve the NANO_SCS-system-based data records for atmospheric and oceanic parameters.

Data availability The Japanese Himawari-8 (H8) and Himawari-9 (H9) geostationary (GEO) satellites are strategically positioned over the South China Sea (SCS), having been launched on October 7, 2014, and November 2, 2016, respectively. It mainly provides cloud mask, fraction, height, phase, optical and microphysical properties, layered precipitable water, and sea surface temperature products, within a temporal resolution of 10 minutes and a gridded resolution of 0.05° × 0.05°. Users can freely access sample HDF-formatted files and data download instruction in PDF format of the South China Sea datasets at https://doi.org/10.6084/m9.figshare.25015853 (Liu Jian, 2024). Besides, for accessing related NRT satellite products, a quick-view website URL is provided: [http://meteorsatellite.hellosea.org.cn/#/index]. Data can be downloaded via FTP (File Transfer Protocol) using the address ftp://www.hellosea.org.cn:10021, with the login credentials being 'smlweix' and the password 'sml#456@'.

623 **Author contributions.** JL and MM contributed to designing the research; MM, JL, and
624 WW implemented the research and wrote the original draft; JL supervised the research;
625 all co-authors revised the paper and contributed to the writing.

626

627 **Competing interests.** The contact author has declared that none of the authors has any
628 competing interests.

629

630 **Disclaimer.** Publisher's note: Copernicus Publications remains neutral with regard to
631 jurisdictional claims in published maps and institutional affiliations.

632

633 **Acknowledgments.** The authors would like to thank JMA, U.S. NASA MODIS group
634 and ECMWF for freely providing Himawari-8/9 (ftp.ptree.jaxa.jp), MODIS
635 (https://search.earthdata.nasa.gov/search), and ERA5 reanalysis
636 (https://cds.climate.copernicus.eu/cdsapp#!/home) data. The authors also would like to
637 thank NOAA for freely providing GFS-NWP
638 (https://nomads.ncep.noaa.gov/pub/data/nccf/com/gfs/) and OISST
639 (https://www.ncei.noaa.gov/data/sea-surface-temperature-optimum-
640 interpolation/v2.1/access/avhrr/) data, and the GOES-R AWG. Besides, we also thanks
641 Dr. Lixin Dong of China National Satellite Meteorological Center who freely provide
642 LST algorithm code. This study was supported by the Southern Marine Science and
643 Engineering Guangdong Laboratory (Zhuhai) (Grant SML2021SP102 and
644 SML2022SP401), National Natural Science Foundation of China under Grants
645 42175086, FengYun Meteorological Satellite Innovation Foundation under Grant FY-
646 APP-ZX-2022.0207, Innovation Group Project of Southern Marine Science and
647 Engineering Guangdong Laboratory (Zhuhai) (No. SML2023SP208). Finally, we
648 would also like to thank the editor and anonymous reviewers for their thoughtful
649 suggestions and comments.

650

651

652

653

654

References

Baum, B. A., P. Yang, S. Nasiri, A. J. Heidinger, A. Heymsfield, and J. Li: Bulk scattering properties from the remote sensing of ice clouds. Part III: High resolution spectral models from 100 to 3250 cm-1, Journal of Applied Meteorology and Climatology, *46*, 423 - 434, doi:10.1175/JAM2473.1, 2007.

Bennartz, R.: Global assessment of marine boundary layer cloud droplet number concentration from satellite, Journal of Geophysical Research - Atmospheres, *112*, D02201, doi:10.1029/2006JD007547, 2007.

Berk, A., G. P. Anderson, P. K. Acharya, J. H. Chetwynd, L. S. Bernstein, E. P. Shettle, M. W. Matthew, and S. M. Adler-Golden (2000), MODTRAN4 user's manual, edited, Air Force Research Laboratory.

Bessho, K., et al.: An introduction to Himawari-8/9—Japan's new-generation geostationary meteorological satellites, Journal of the Meteorological Society of Japan, *94*, 151-183, doi:10.2151/jmsj.2016-009, 2016.

Cai, W., B. Ng, G. Wang, A. Santoso, L. Wu, and K. Yang: Increased ENSO sea surface temperature variability under four IPCC emission scenarios, Nature Climate Change, *12*, 228–231, 2022.

Charlesworth, E., et al.: Stratospheric water vapor affecting atmospheric circulation, Nature Communications, *14*, 3925, doi:10.1038/s41467-023-39559-2, 2023.

Chou, M.-D., M. J. Suarez, C.-H. Ho, M. M.-H. Yan, and K.-T. Lee: Parameterizations for cloud overlapping and shortwave single-scattering properties for use in general circulation and cloud ensemble models, J Climate, *11*, 202-214, doi:10.1175/1520-0442(1998)011<0202:PFCOAS>2.0.CO;2, 1998.

Ding, Y., and Y. Liu: Onset and the evolution of the Summer Monsoon over the South China Sea during SCSMEX Field Experiment in 1998, Journal of the Meteorological Society of Japan, *V79*, 255-276, doi:10.2151/jmsj.79.255, 2001.

Dong, L., S. Tang, F. Wang, M. Cosh, X. Li, and M. Min: Inversion and validation of FY-4A official land surface temperature product, Remote Sensing, *15*, 2437, doi:10.3390/rs15092437 2023.

Fernando, M., Millangoda, M., and Premalal, S.: Analyze and Comparison of the Atmospheric Instability Using K-Index, Lifted Index Total Totals Index Convective Availability Potential Energy (CAPE) and Convective Inhibition (CIN) in Development of Thunderstorms in Sri Lanka During Second Inter-Monsoon, Multi-Hazard Early Warning and Disaster Risks, Cham, 2021//, 603-614,

Gu, Y., Brown, J. F., Verdin, J. P., and Wardlow, B. D.: A five-year analysis of MODIS NDVI and NDWI for grassland drought assessment over the central Great Plains of the United States, Geophysical Research Letters, 34, 2007.

Hall, D. K., Riggs, G. A., and Salomonson, V. V.: Development of methods for mapping global snow cover using moderate resolution imaging spectroradiometer data, Remote Sensing of Environment, 54, 127-140, 1995.

Heidinger, A., and M. Pavolonis: Gazing at cirrus clouds for 25 years through a split window, part 1: Methodology, Journal of Applied Meteorology and Climatology, *48*, 1110-1116, doi:10.1175/2008JAMC1882.1, 2009.

Heidinger, A. K., A. T. Evan, M. J. Foster, and A. Walther: A naive Bayesian cloud-

detection scheme derived from CALIPSO and applied within PATMOS-x, Journal of Applied Meteorology and Climatology, *51*, 1129–1144, doi:10.1175/JAMC-D-11-02.1, 2012.

Hersbach, H., et al.: The ERA5 global reanalysis, Quarterly Journal of the Royal Meteorological Society, *146*, 1999–2049, doi:10.1002/qj.3803, 2020.

Heymsfield, A. J., S. Matrosov, and B. Baum: Ice water path-optical depth relationships for cirrus and deep stratiform ice cloud layers, J Appl Meteorol, *42*, 1369–1390, doi:10.1175/1520-0450(2003)042<1369:IWPDRF>2.0.CO;2, 2007.

Hong, F., W. Zhan, F.-M. Göttsche, Z. Liu, P. Dong, H. Fu, F. Huang, and X. Zhang: A global dataset of spatiotemporally seamless daily mean land surface temperatures: generation, validation, and analysis, Earth System Science Data, *14*, 3091–3113, doi:10.5194/essd-14-3091-2022, 2022.

Huang, B., C. Liu, V. Banzon, E. Freeman, G. Graham, B. Hankins, T. Smith, and H.-M. Zhang: Improvements of the Daily Optimum Interpolation Sea Surface Temperature (DOISST) Version 2.1, J Climate, *34*, 2923-2939, doi:10.1175/JCLI-D-20-0166.1, 2021.

Husi, L., T. M. Nagao, T. Y. Nakajima, J. Riedi, H. Ishimoto, A. J. Baran, H. Shang, M. Sekiguchi, and M. Kikuchi: Ice cloud properties from Himawari-8/AHI next-generation geostationary satellite: Capability of the AHI to monitor the DC cloud generation process, IEEE Transactions on Geoscience and Remote Sensing, *57*, 3229-3239, doi:10.1109/TGRS.2018.2882803 2019.

Jiang, J., T. Zhou, Y. Qian, C. Li, F. Song, H. Li, X. Chen, W. Zhang, and Z. Chen: Precipitation regime changes in High Mountain Asia driven by cleaner air, Nature, doi:10.1038/s41586-023-06619-y, 2023.

Kim, D., M. Gu, T.-H. Oh, E.-K. Kim, and H.-J. Yang: Introduction of the advanced meteorological imager of Geo-Kompsat-2a: In-orbit tests and performance validation, Remote Sensing, *13*, 1303, doi:10.3390/rs13071303, 2021.

King, M. D., S. C. Tsay, S. E. Planick, M. Wang, and K. N. Liou: Cloud retrieval algorithms: Optical thickness, effective particle radius, and thermodynamic phase, NASA MODIS Algorithm Theoretical Basis Documents, 1997.

Koseki, S., K. Tieh-Yong, and T. Chee-Kiat: Effects of the cold tongue in the South China Sea on the monsoon, diurnal cycle and rainfall in the Maritime Continent, Quarterly Journal of the Royal Meteorological Society, *139*, 1566-1582, doi:10.1002/qj.2052, 2013.

Lai, R., S. Teng, B. Yi, H. Letu, M. Min, S. Tang, and C. Liu: Comparison of cloud properties from Himawari-8 and FengYun-4A geostationary satellite radiometers with MODIS cloud retrievals, Remote Sensing, *11*, 1703, doi:10.3390/rs11141703, 2019.

Letu, H., T. M. Nagao, T. Y. Nakajima, J. Riedi, H. Ishimoto, A. J. Baran, H. Shang, M. Sekiguchi, and M. Kikuchi: Ice cloud properties from Himawari-8/AHI next-generation geostationary satellite: Capability of the AHI to monitor the DC cloud generation process, IEEE Transactions on Geoscience and Remote Sensing, *57*, 3229-3239, doi:10.1109/tgrs.2018.2882803, 2019.

Letu, H., et al.: High-resolution retrieval of cloud microphysical properties and surface solar radiation using Himawari-8/AHI next-generation geostationary satellite, Remote Sensing of Environment, *239*, 111583, doi:10.1016/j.rse.2019.111583, 2020.

Levenberg, K.: A method for the solution of certain non-linear problems in least squares, Quarterly of Applied Mathematics, *2*, 164-168, 1944.

Li, J., W. P. Menzel, T. J. Schmit, and J. Schmetz: Applications of geostationary hyperspectral infrared sounder observations – progress, challenges, and future perspectives, Bulletin of the American Meteorological Society, doi:10.1175/BAMS-D-21-0328.1, 2022a.

Li, J., T. J. Schmit, X. Jin, and G. Martin: GOES-R Advanced Baseline Imager (ABI) Algorithm Theoretical Basis Document For Legacy Atmospheric Moisture Profile, Legacy Atmospheric Temperature Profile, Total Precipitable Water, and Derived Atmospheric Stability Indices NOAA Goes-R ATBD, 109, 2012.

Li, J., P. Wang, H. Han, J. Li, and J. Zheng: On the assimilation of satellite sounder data in cloudy skies in numerical weather prediction models, Journal of Meteorological Research, *30*, 169–182, 2016.

Li, J., W. W. Wolf, W. P. Menzel, W. Zhang, H.-L. Huang, and T. H. Achtor: Global soundings of the atmosphere from ATOVS measurements: The algorithm and validation, Journal of Applied Meteorology, *39*, 1248–1268, doi:10.1175/1520-0450(2000)039<1248:GSOTAF>2.0.CO;2, 2000.

Li, Y., G. Ren, Q. Wang, L. Mu, and Q. Niu: Marine heatwaves in the South China Sea: Tempo-spatial pattern and its association with large-scale circulation, Remote Sensing, *14*, 5829, doi:10.3390/rs14225829, 2022b.

Liang, Y., M. Min, Y. Yu, X. Wang, and P. Xia: Assessing diurnal cycle of cloud covers of Fengyun-4A geostationary satellite based on the manual observation data in China, IEEE Transactions on Geoscience and Remote Sensing, *61*, doi:10.1109/TGRS.2023.3256365, 2023.

Liu, B., Y. Liu, G. Wu, J. Yan, J. He, and S. Ren: Asian summer monsoon onset barrier and its formation mechanism, Climate Dynamics, *45*, 711–726, doi:10.1007/s00382-014-2296-0, 2014.

Liu Jian, Y. J., Lin Chuyong, He Min, Liu Haiyan, Min Min, Wang Wei (2024), Near real-time atmospheric and oceanic science products of Himawari-8/9 geostationary satellites over the South China Sea, edited, figshare. Dataset., doi:https://doi.org/10.6084/m9.figshare.25015853.

Ma, Z., J. Li, W. Han, Z. Li, Q. Zeng, W. P. Menzel, T. J. Schmit, D. Di, and C.-Y. Liu: Four‐dimensional wind fields from geostationary hyperspectral infrared sounder radiance measurements with high temporal resolution, Geophys Res Lett, *48*, e2021GL093794, doi:10.1029/2021GL093794, 2021.

Martin, D. W., and M. R. Howland: Rainfall over the Arabian Sea during the onset of the 1979 monsoon, Nature, *300*, 628–630, 1982.

Min, M., et al.: Estimating summertime precipitation from Himawari-8 and global forecast system based on machine learning, IEEE Transactions on Geoscience

and Remote Sensing, *57*, 2557-2570, doi:10.1109/TGRS.2018.2874950, 2019.

Min, M., B. Chen, N. Xu, X. He, X. Wei, and M. Wang: Nonnegligible diurnal and long-term variation characteristics of the calibration biases in Fengyun-4A/AGRI infrared channels based on the oceanic drifter data, IEEE Transactions on Geoscience and Remote Sensing, *60*, 1-15, doi:10.1109/TGRS.2022.3160450, 2022.

Min, M., J. Deng, C. Liu, N. Lu, X. Hu, L. Chen, J. Guo, P. Zhang, Q. Lu, and L. Wang: An investigation of the implications of lunar illumination spectral changes for Day/Night Band based cloud property retrieval due to lunar phase transition, Journal of Geophysical Research: Atmospheres, *122*, 9233-9244, doi:10.1002/2017JD027117, 2017a.

Min, M., J. Li, F. Wang, Z. Liu, and W. P. Menzel: Retrieval of cloud top properties from advanced geostationary satellite imager measurements based on machine learning algorithms, Remote Sensing of Environment, *239*, 111616, doi:10.1016/j.rse.2019.111616 2020.

Min, M., et al.: Developing the science product algorithm testbed for Chinese next-generation geostationary meteorological satellites: Fengyun-4 series, Journal of Meteorological Research, *31*, 708-719, doi:10.1007/s13351-017-6161-z, 2017b.

Mülmenstädt, J., M. Salzmann, J. E. Kay, M. D. Zelinka, P.-L. Ma, C. Nam, J. Kretzschmar, S. Hörnig, and J. Quaas: An underestimated negative cloud feedback from cloud lifetime changes, Nature Climate Change, *11*, 508–513, doi:10.1038/s41558-021-01038-1, 2021.

Nakajima, T., and M. D. King: Determination of the optical thickness and effective particle radius of clouds from reflected solar radiation measurements. Part I: Theory, J Atmos Sci, *48*, 728-750, 1990.

Niu, Q., and Y. Feng: Relationships between the typhoon-induced wind and waves in the northern South China Sea, Geophys Res Lett, *48*, e2020GL091665, doi:10.1029/2020GL091665, 2021.

Noh, Y.-J., J. M. Forsythe, S. D. Miller, C. J. Seaman, Y. Li, A. K. Heidinger, D. T. Lindsey, M. A. Rogers, and P. T. Partain: Cloud-base height estimation from VIIRS. Part II: A statistical algorithm based on A-Train satellite data, Journal of Atmospheric and Oceanic Technology, *34*, 585–598, doi:10.1175/JTECH-D-16-0110.1, 2017.

Parol, F., J. C. Buriez, G. Brogniez, and Y. Fouquart: Information content of AVHRR channels 4 and 5 with respect to the effective radius of cirrus cloud particles, J Appl Meteorol, *30*, 973–984, 1991.

Pavolonis, M.: GOES-R Advanced Baseline Imager (ABI) Algorithm Theoretical Basis Document For Cloud Type and Cloud Phase Version 2.0, NOAA GOES-R ATBD, 1-96, 2010a.

Pavolonis, M. J.: Advances in extracting cloud composition information from spaceborne infrared radiances-A robust alternative to brightness temperatures. Part I: Theory, Journal of Applied Meteorological Climatology, *49*, 1992-2012, 2010b.

Pavolonis, M. J., A. K. Heidinger, and T. Uttal: Daytime global cloud typing from AVHRR and VIIRS: Algorithm description, validation, and comparisons J Appl Meteorol, *44*, 804-826, 2005.

Platnick, S., M. D. King, S. A. Ackerman, W. P. Menzel, B. A. Baum, J. C. Riédi, and R. A. Frey: The MODIS cloud products: Algorithms and examples from Terra, IEEE Transactions on Geoscience and Remote Sensing, *41*, 459-473, doi:10.1109/TGRS.2002.808301, 2003.

Platnick, S., et al.: The MODIS cloud optical and microphysical products: Collection 6 updates and examples from Terra and Aqua, IEEE Transactions On Geoscience and Remote Sensing, *55*, 502-525, doi:10.1109/TGRS.2016.2610522, 2017.

Reynolds, R., T. M. Smith, C. Liu, D. Chelton, K. Casey, and M. Schlax: Daily high-resolution-blended analyses for sea surface temperature, J Climate, *20*, 5473-5496, doi:10.1175/2007JCLI1824.1, 2007.

Rodgers, C. D.: Inverse methods for atmospheric sounding: Theory and practice, 2000.

Schmit, T. J., P. Griffith, M. M. Gunshor, J. M. Daniels, S. J. Goodman, and W. J. Lebair: A closer look at the ABI on the GOES-R Series Bulletin of the American Meteorological Society, *98*, 681-698 doi:10.1175/BAMS-D-15-00230.1, 2017.

Soldi, G., et al.: Space-based global maritime surveillance. Part I: Satellite technologies, IEEE Aerospace and Electronic Systems Magazine *36*, 8-28, doi:10.1109/MAES.2021.3070862, 2021.

Ulivieri, C., and G. Cannizzaro: Land surface temperature retrievals from satellite measurements, Acta Astronaut, *12*, 985–997, doi:10.1016/0094-5765(85)90026-8, 1985.

Viúdez-Mora, A., C.-S. M., J. Calbó, and J. A. González: Modeling atmospheric longwave radiation at the surface during overcast skies: The role of cloud base height, Journal of Geophysical Research: Atmospheres, *120*, 199-214, doi:10.1002/2014JD022310, 2015.

Walther, A., W. Straka, and A. K. Heidinger: GOES-R Advanced Baseline Imager (ABI) algorithm theoretical basis document for daytime cloud optical and microphysical properties (DCOMP), NOAA Goes-R ATBD, 2011.

Walton, C. C., W. G. Pichel, J. F. Sapper, and D. A. May: The development and operational application of nonlinear algorithms for the measurement of sea surface temperatures with the NOAA polar-orbiting environmental satellites, Journal of Geophysical Research, *103*, 27999-28012, doi:10.1029/98JC02370, 1998.

Wang, B., F. Huang, Z. Wu, J. Yang, X. Fu, and K. Kikuchi: Multi-scale climate variability of the South China Sea monsoon: A review, Dynamics of Atmospheres and Oceans, *47*, 15-37, doi:10.1016/j.dynatmoce.2008.09.004, 2009.

Wang, F., M. Min, N. Xu, C. Liu, Z. Wang, and L. Zhu: Effects of linear calibration errors at low temperature end of thermal infrared band: Lesson from failures in cloud top property retrieval of FengYun-4A geostationary satellite, IEEE Transactions on Geoscience and Remote Sensing, *60*, 5001511,

872   doi:10.1109/TGRS.2022.3140348, 2022.

873 Wang, G., S.-P. Xie, T. Qu, and R. X. Huang: Deep South China Sea circulation,
874   Geophys Res Lett, *38*, L05601, doi:10.1029/2010GL046626, 2011.

875 Wang, M., M. Min, J. Li, B. Chen, H. Lin, Z. Yao, N. Xu, and M. Zhang: Applicability
876   of physics-based and machine-learning-based algorithms of geostationary
877   satellite in retrieving the diurnal cycle of cloud base height, Atmospheric
878   Chemistry and Physics Discussion, 2024.

879 Wang, X., Q.-Y. Liu, D. Sui, and D. Wang: The imprint of the ENSO activities on the
880   South China Sea wave climate, Ocean Dynamics, *70*, 1315–1323,
881   doi:10.1007/s10236-020-01400-5, 2020.

882 Wang, X., M. Min, F. Wang, J. Guo, B. Li, and S. Tang: Intercomparisons of cloud mask
883   product among Fengyun-4A, Himawari-8 and MODIS, IEEE Transactions on
884   Geoscience and Remote Sensing, *57*, 8827-8839,
885   doi:10.1109/TGRS.2019.2923247 2019.

886 Whitaker, J. S., T. M. Hamill, X. Wei, Y. Song, and Z. Toth: Ensemble data assimilation
887   with the NCEP global forecast system, Monthly Weather Review, *136*, 463–482,
888   doi:10.1175/2007MWR2018.1, 2008.

889 Xia, P., M. Min, Y. Yu, Y. Wang, and L. Zhang: Developing a near real-time cloud cover
890   retrieval algorithm using geostationary satellite observations for photovoltaic
891   plants, Remote Sensing, *15*, 1141, doi:10.3390/rs15041141, 2023.

892 Xia, P., L. Zhang, M. Min, J. Li, Y. Wang, Y. Yu, and S. Jia: Accurate nowcasting on
893   cloud cover at solar photovoltaic plants using geostationary satellite images,
894   Nature Communications, *15*, 1-10, doi:10.1038/s41467-023-44666-1, 2024.

895 Xiao, X., Boles, S., Frolking, S., Li, C., Babu, J. Y., Salas, W., and Moore, B.: Mapping
896   paddy rice agriculture in South and Southeast Asia using multi-temporal
897   MODIS images, Remote Sensing of Environment, *100*, 95-113,
898   https://doi.org/10.1016/j.rse.2005.10.004, 2006.

899 Xu, W., S. A. Rutledge, and K. Chudler: Diurnal cycle of coastal convection in the
900   South China Sea region and modulation by the BSISO*34*, 4297–4314,
901   doi:10.1175/JCLI-D-20-0308.1, 2021.

902 Yang, J., Z. Zhang, C. Wei, F. Lu, and Q. Guo: Introducing the new generation of
903   Chinese geostationary weather satellites, FengYun-4, Bulletin of the American
904   Meteorological Society, *98*, 1637-1658, doi:10.1175/BAMS-D-16-0065.1,
905   2017.

906 Zhao, G., and L. D. Girolamo: Cloud fraction errors for trade wind cumuli from EOS-
907   Terra instruments, Geophys Res Lett, *33*, L20802, doi:10.1029/2006GL027088,
908   2006.

909 Zheng, J., J. Li, T. J. Schmit, J. Li, and Z. Liu: The impact of AIRS atmospheric
910   temperature and moisture profiles on hurricane forecasts: Ike (2008) and Irene
911   (2011), Advances in Atmospheric Sciences, *32*, 319–335, 2015.

912 Zheng, Y., L. Tang, and H. Wang: An improved approach for monitoring urban built-up
913   areas by combining NPP-VIIRS nighttime light, NDVI, NDWI, and NDBI,
914   Journal of Cleaner Production, *328*, 129488, doi:10.1016/j.jclepro.2021.129488,

915   2021.

916   Zhou, R., X. Pan, Z. Xiaohu, X. Na, and M. Min: Research progress and prospects of
917   atmospheric motion vector based on meteorological satelliteimages, Reviews of
918   Geophysics   and   Planetary   Physics   (In   Chinese),   *55*,   184-194,
919   doi:10.19975/j.dqyxx.2022-077, 2024.

920   Zhu, L., R. Zhou, D. Di, W. Bai, and Z. Liu: Retrieval of atmospheric water vapor
921   content in the rnvironment from AHI/H8 using both physical and random forest
922   methods—A case study for typhoon Maria (201808), Remote Sensing, *15*, 498,
923   doi:10.3390/rs15020498, 2023.

924
925

926

927

928

929

930

931

932

933

934

935

936

937

938

939

940

941

942

943

944

Tables and Figures

Table 1. Primary NRT H8/9 GEO satellite atmospheric and oceanic science products and related variables generated by the NANO_SCS system.

Product Name (Abbr.)	Variable Name	Valid Value	Unit	Note
Cloud Mask (CLM)	Cloud_Mask	0=Cloudy; 1=Probably cloudy; 2=Probably clear ; 3=Clear	None	
Cloud Fraction (CLF)	Cloud_Fraction	0-100	%	down-sampled 5×5 pixel box
Cloud Type and Phase (CLP)	Cloud_Type	0=Clear; 1=Spare; 2=Liquid water; 3=Supercooled water; 4=Mixed; 5=Optically thick ice; 6=Optically thin ice; 7=Multilayered ice; 8=Uncertainty	None	1=Spare: pixel with spare cloud cover
	Cloud_Phase	0=Clear; 1=Liquid water; 2=Supercooled water; 3=Mixed; 4=Ice; 5=Uncertainty	None	
Cloud Top Properties (CTP)	Cloud_Top_Height	0-30000	m	
	Cloud_Top_Pressure	0-2000	hPa	
	Cloud_Top_Temperature	0-400	K	
	Cloud_Emissivity_at_11μm	0-100	%	
Cloud Optical and Microphysical Properties (COT)	Cloud_Optical_Depth	0-150	None	only daytime
	Cloud_Effective_Radius	0-100	μm	only daytime
	Cloud_Liquid_Water_Path	0-1000	g/m^2	only daytime
	Cloud_Ice_Water_Path	0-1000	g/m^2	only daytime
Cloud Base Properties (CBP)	Cloud_Base_Height	0-30000	m	only daytime
	Cloud_Base_Pressure	0-2000	hPa	only daytime
Sea Surface Temperature (SST)	Sea_Surface_Temperature	0-400	K	
Land Surface Temperature (LST)	Land_Surface_Temperature	0-400	K	
Vegetation/Water Indices (NDI)	NDVI (Normalized Difference Vegetation Index)	0-1.0	None	only daytime
	NDSI (Normalized Differential Snow Index)	0-1.0	None	only daytime
	NDWI (Normalized Differential Water Index)	0-1.0	None	only daytime
	LSWI (Land Surface Water Index)	0-1.0	None	only daytime
Layered Precipitable Water (LPW)	Total_Precipitable_Water	0-1000	mm	
	Water_Vapor_High	0-1000	mm	700-300hPa
	Water_Vapor_Middle	0-1000	mm	900-700hPa
	Water_Vapor_Low	0-1000	mm	Surface-900hPa
	CAPE_Index (Convective Available Potential Energy)	0-10000	J/kg	
	K_Index	-100-100	K	
	LI_Index (Lifted)	-100-100	ºC	
	Showalter_Index	-100-100	ºC	
	TT_Index (Total totals)	-100-100	ºC	

948

949

950

951
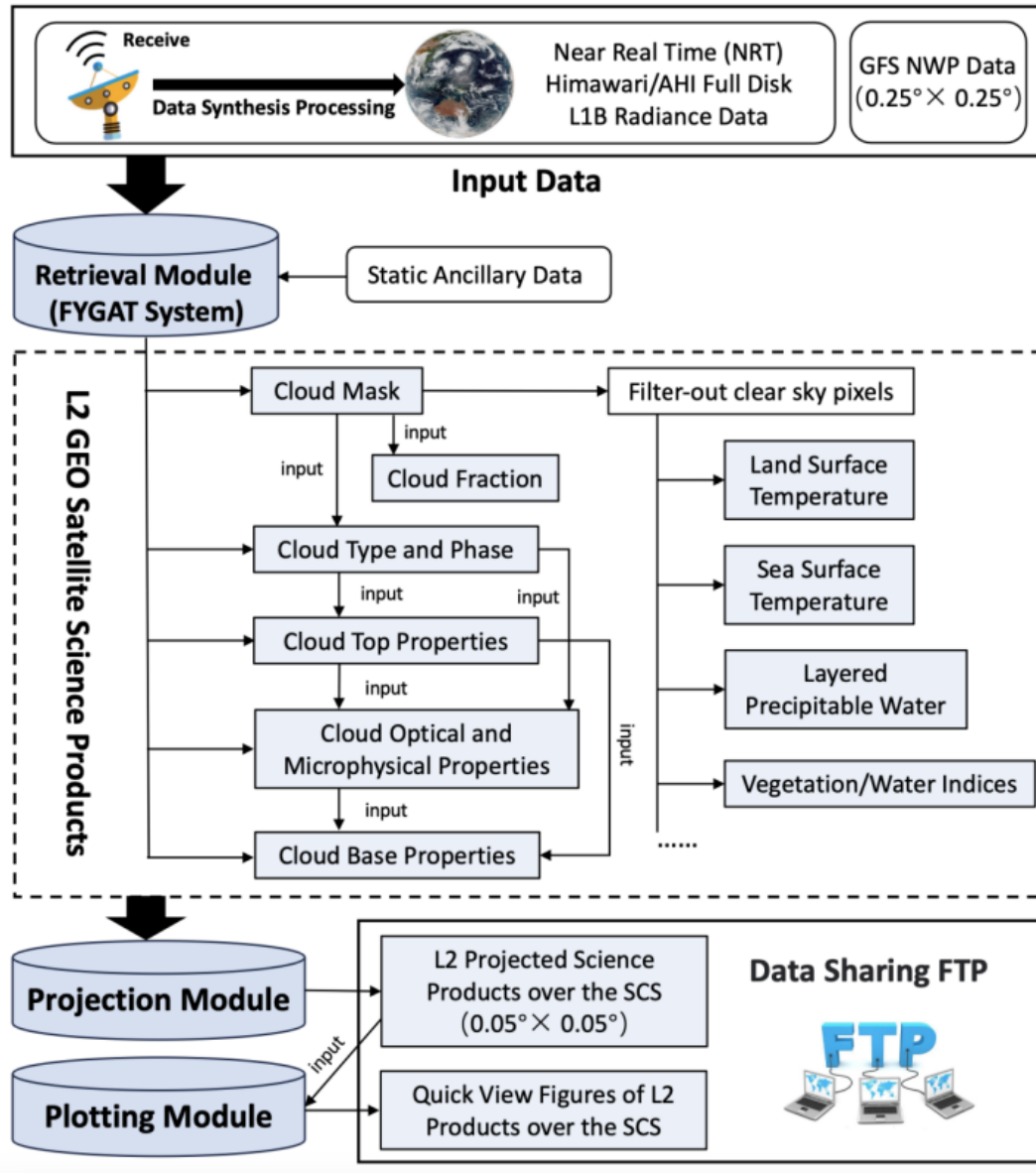
Figure 1. Flowchart of the NANO_SCS system. Dark gray shading represents key processing module; light gray shading represents satellite science product.

955

956

957

958

959

960

961
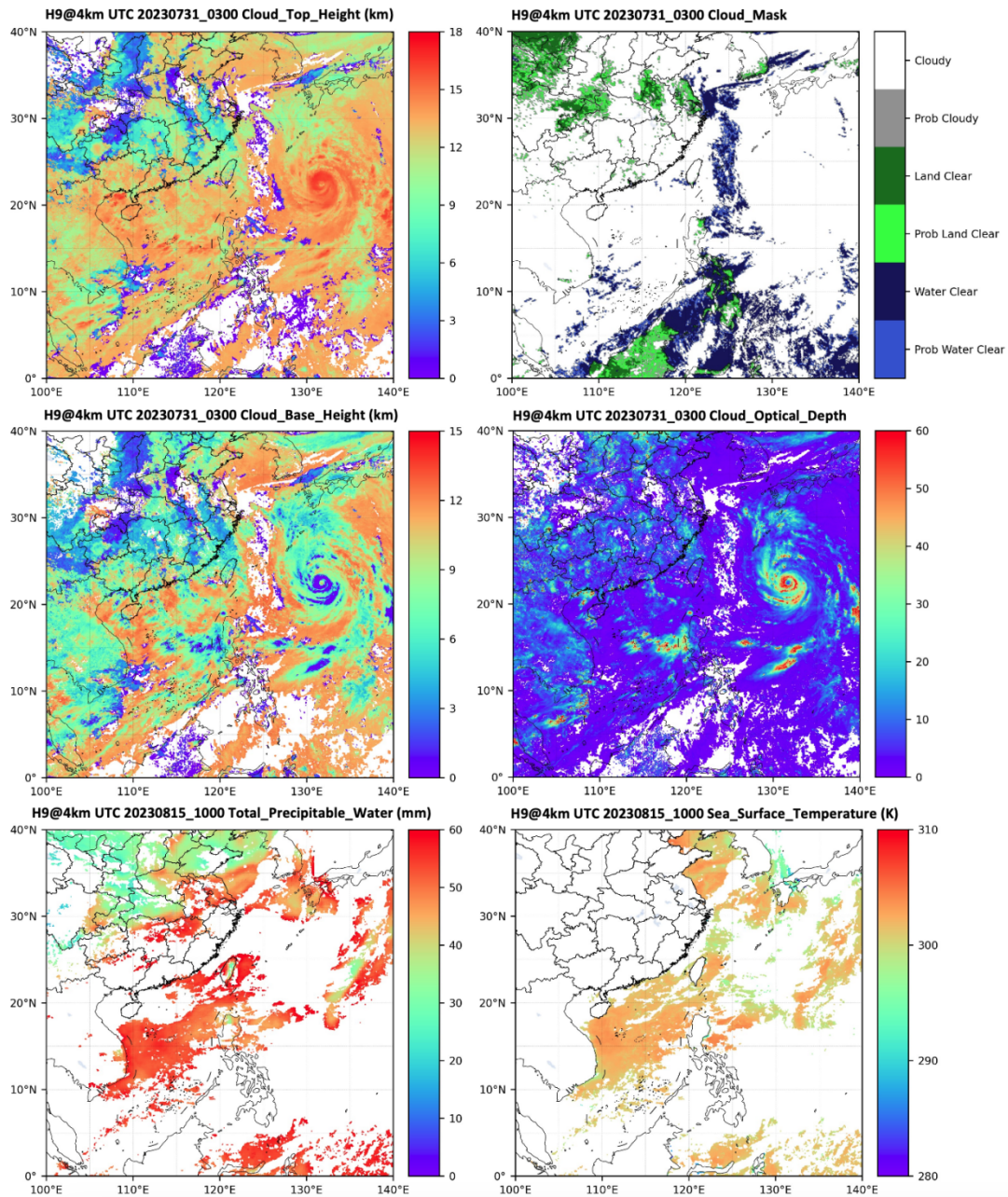
Figure 2. H9/AHI GEO satellite cloud top height (left top panel), cloud mask (right top panel), cloud base height (left middle panel), cloud optical depth (right middle panel) at 03:00 UTC on July 31, 2023, and atmospheric total precipitable water (left bottom panel) and sea surface temperature (right bottom panel) at 10:00 UTC on August 15, 2023 over the NANO_SCS system.

968

969

970

971

Figure 3. Cloud mask comparisons between (a, c) H9/AHI GEO satellite and (b, d) MODIS at 05:10 (top panel) and 17:20 (middle panel) UTC on January 8, 2023. (e) POD, FAR, HR, and KSS scores of H9/AHI results for all the matched pixels over land (earthy yellow) and sea (blue) in January, April, July, and October of 2023. "clr" and "cld" respectively signify the clear-sky and cloudy-sky pixels.
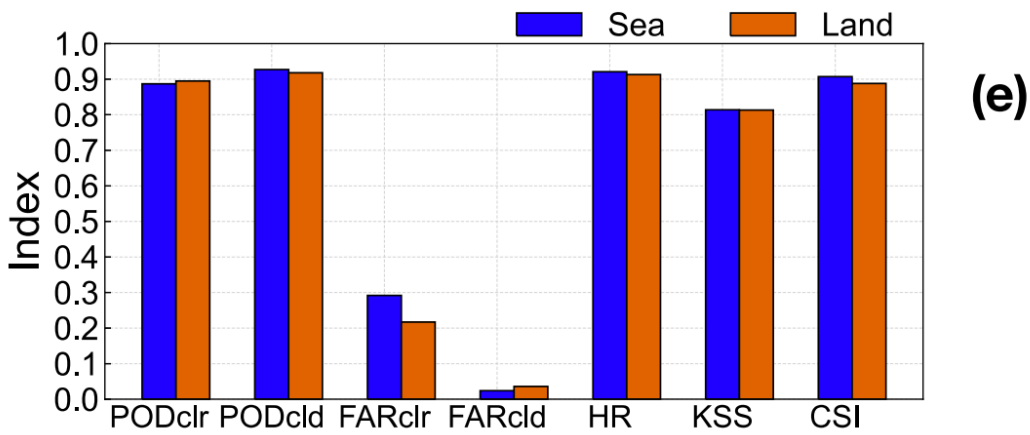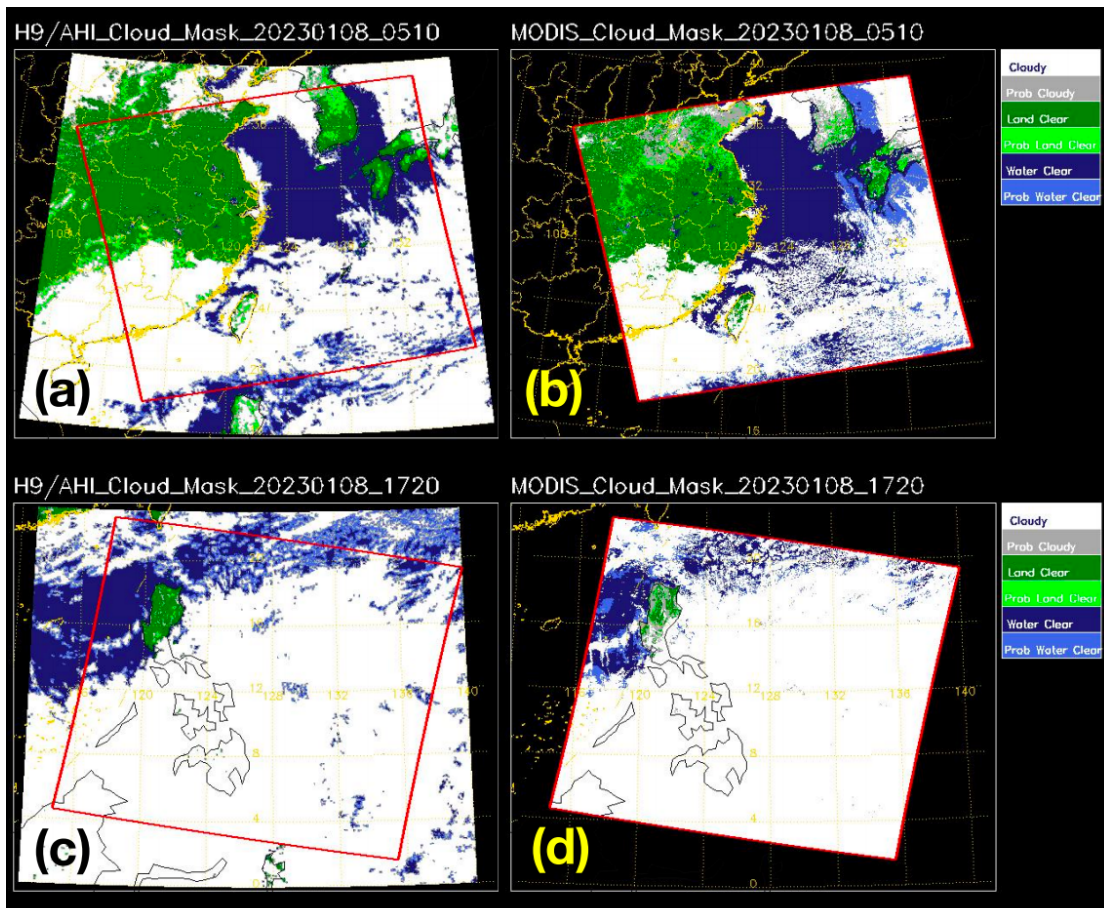
972
973
974
975
976

977
978
979
980

981

982
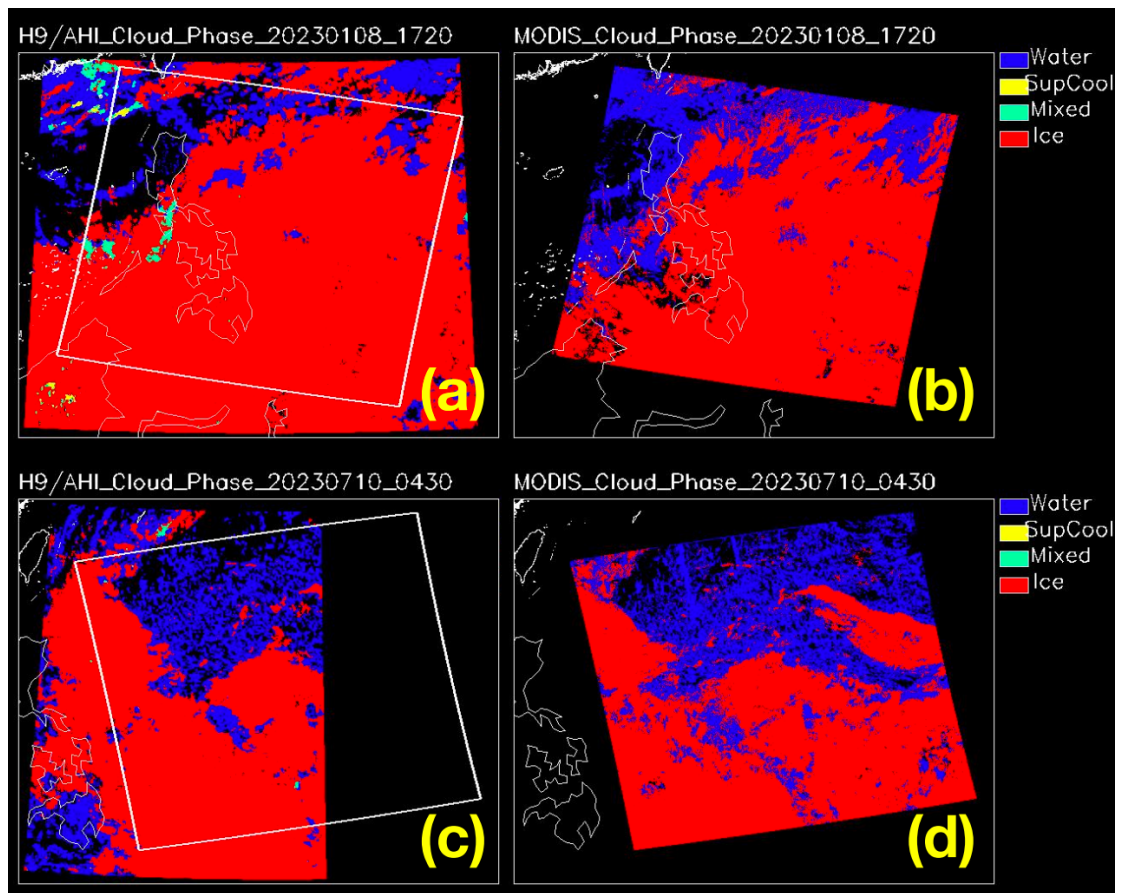
Figure 4. Cloud phase comparisons between (a, c) H9/AHI GEO satellite and (b, d)
MODIS at 05:10 UTC (top panel) on January 8, 2023 and 04:30 UTC (bottom panel)
on July 10, 2023.

986

987

988

989

990

991

992

993

994

995

996

997

998

999

1000
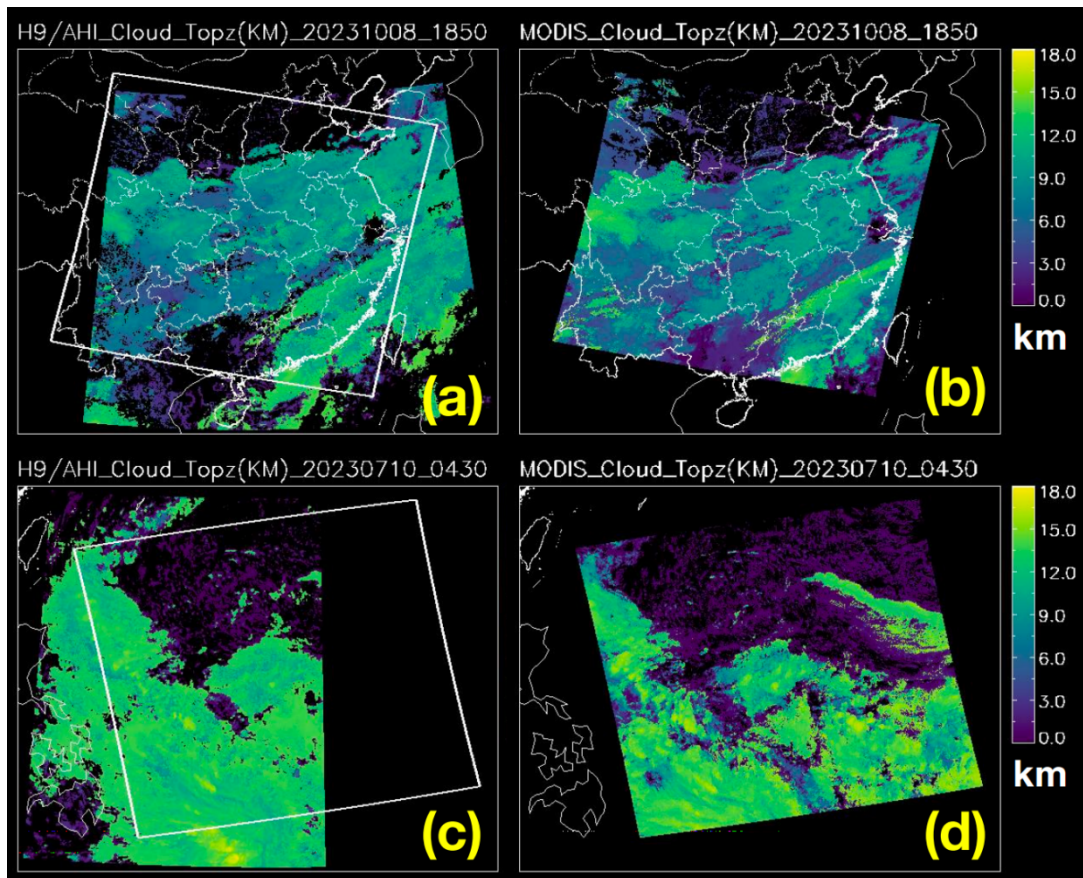
1001

Figure 5. Cloud top height comparisons between (a, c) H9/AHI GEO satellite and (b,
d) MODIS at 18:50 UTC (top panel) on October 8, 2023 and 04:30 UTC (bottom panel)
on July 10, 2023.

1005

1006

1007

1008

1009

1010

1011

1012

1013

1014

1015

1016

1017

1018
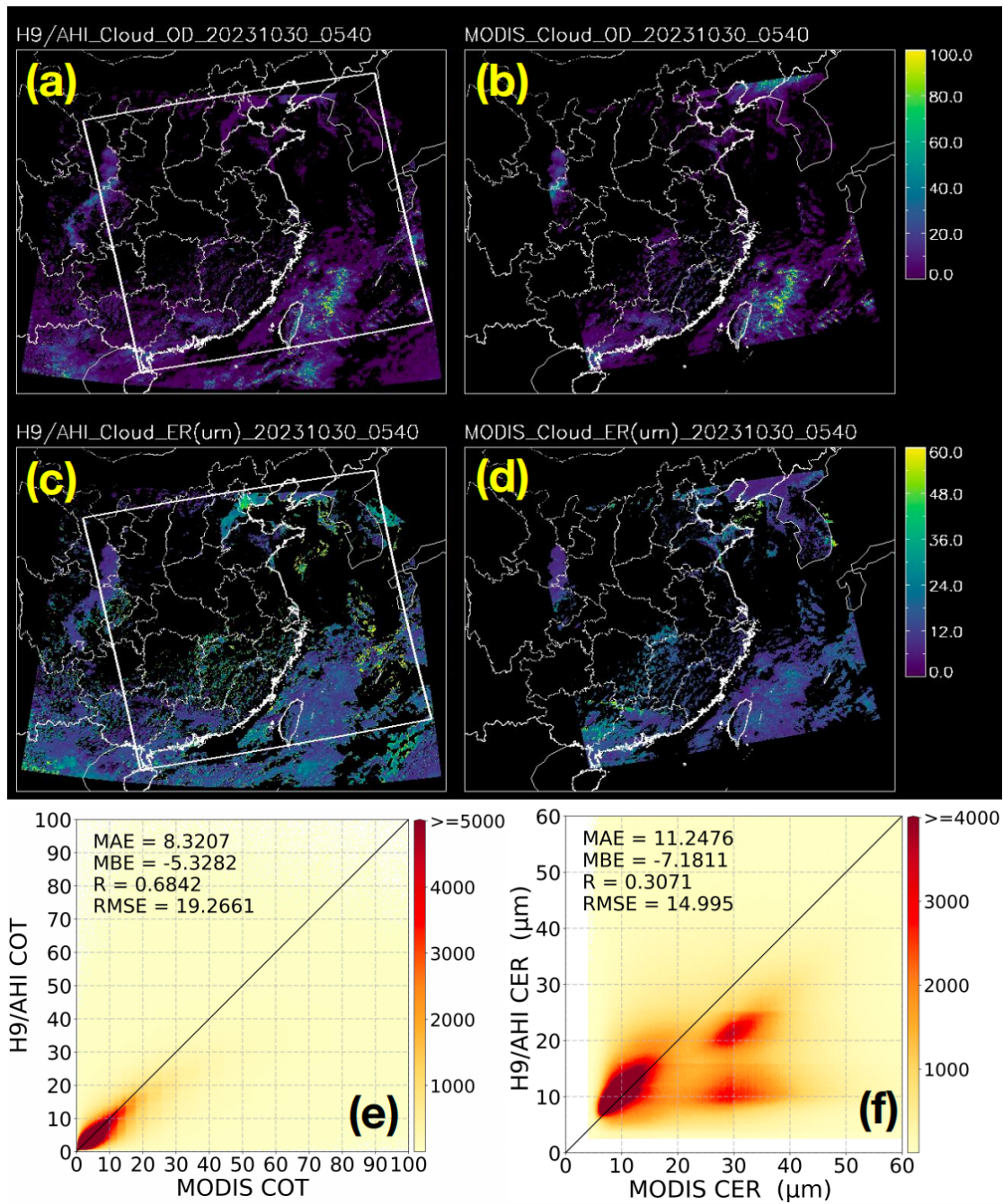
1019

1020 **Figure 6.** Cloud optical depth (top panel) and effective radius (middle panel)

1021 comparisons between (a, c) H9/AHI GEO satellite and (b, d) MODIS at 05:40 UTC on

1022 October 30, 2023. Comparisons of the one year (2023) (e) cloud optical depth and (f)

1023 effective radius from MODIS and H9/AHI data over the NANO_SCS system. The color

1024 bar represents the total number in every bin at an interval of 0.2 of COT or 0.2 μm of

1025 CER.

1026
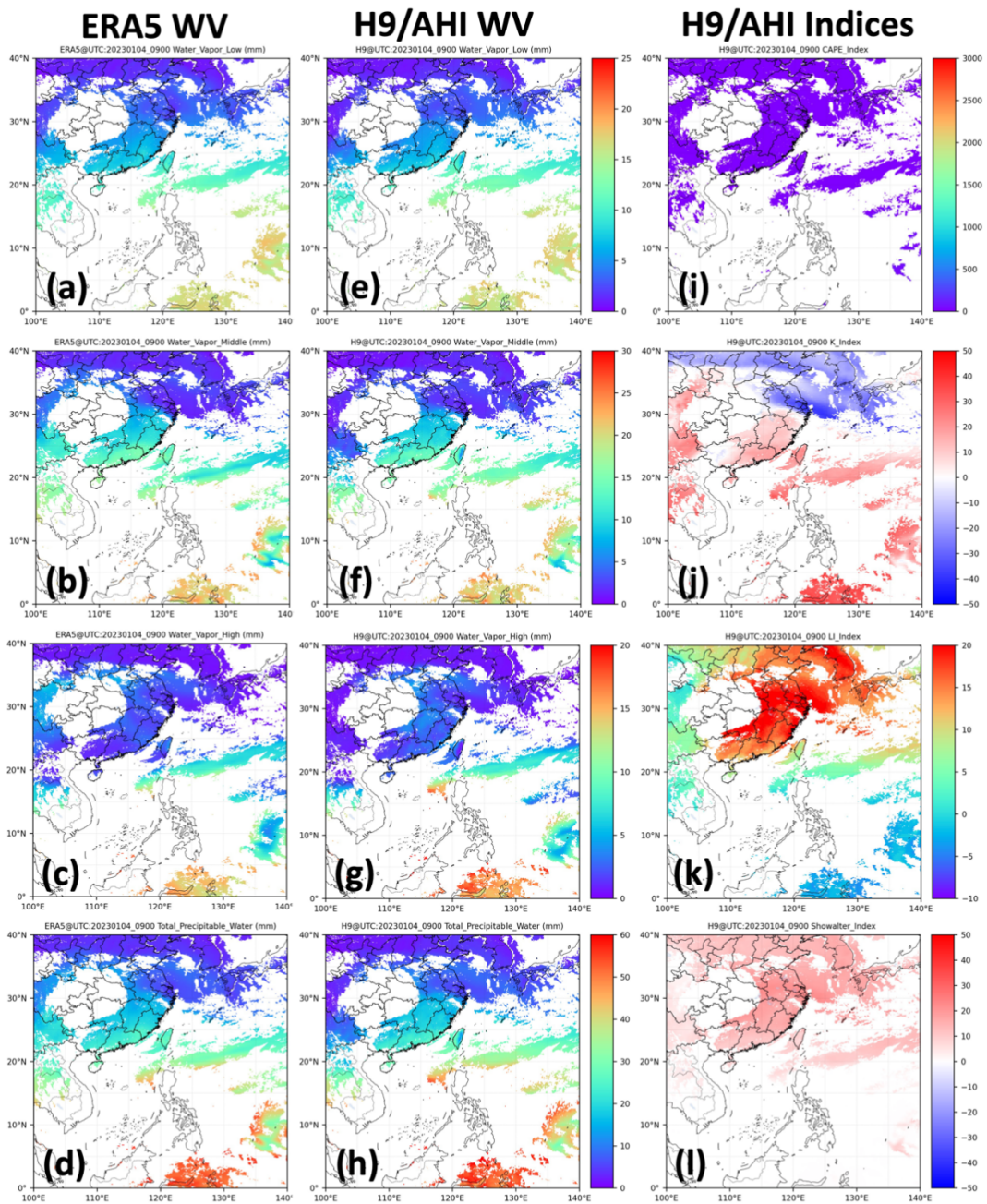
Figure 7. ERA5 (first column panel) and H9/AHI GEO satellite (middle column panel) atmospheric (a, e) water vapor at low layer (Surface-900hPa), (b, f) water vapor at middle layer (900-700hPa), (c, g) water vapor at high layer (700-300hPa), (d, h) total precipitable water, (i) H9/AHI CAPE index, (j) H9/AHI K index, (k) H9/AHI LI index, and (l) H9/AHI Showalter index at 09:00 UTC on January 4, 2023 over the NANO_SCS system.

1035

1036

1037
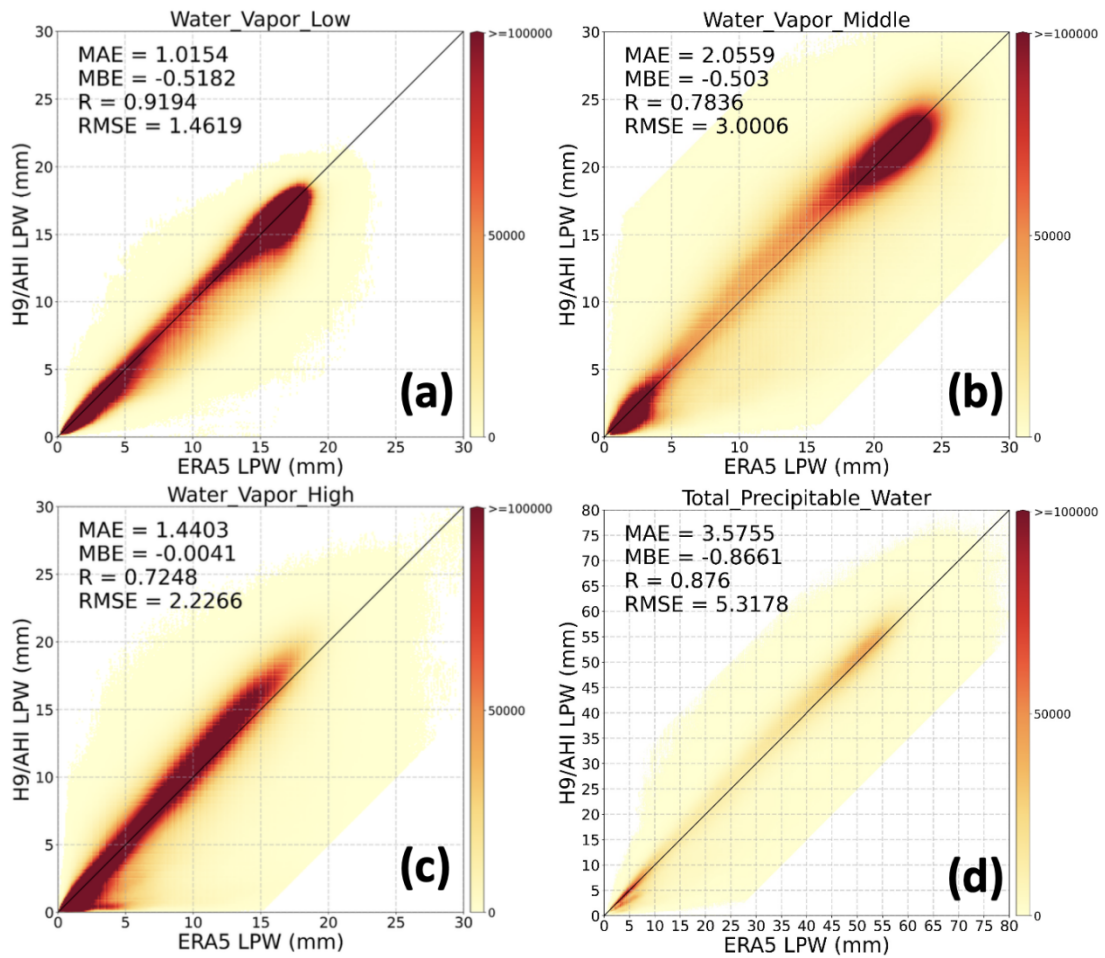
1038

1039   **Figure 8.** Comparisons of the one year (2023) layered precipitable water (LPW) values

1040   (a, Low; b, Middle; c, High; d, Total) from ERA5 reanalysis and H9/AHI data over the

1041   NANO_SCS system. The color bar represents the total number in every bin at an

1042   interval of 0.1 mm.

1043

1044

1045

1046

1047

1048

1049

1050

1051

1052

1053

1054
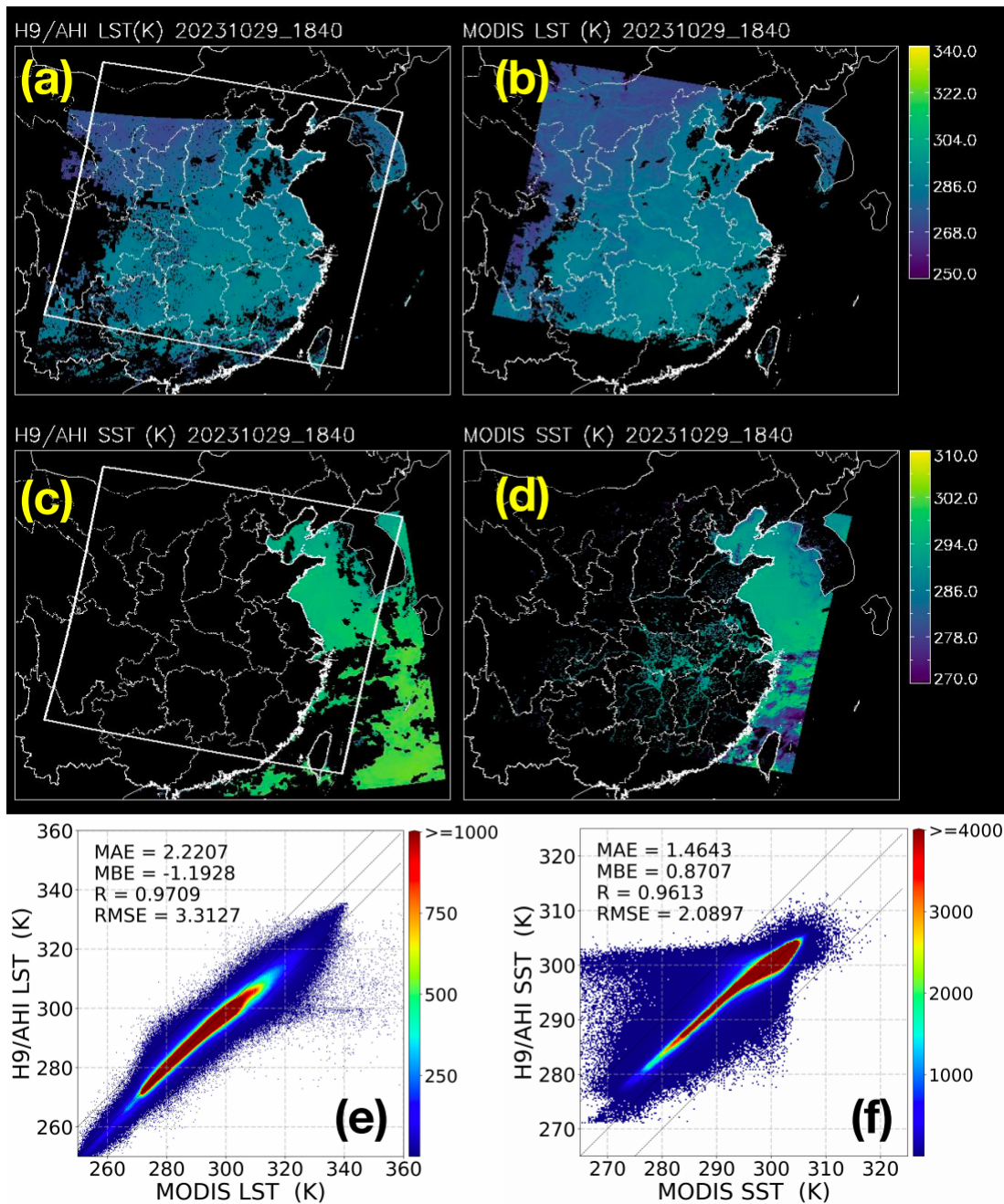
1055

1056 **Figure 9.** LST (top panel) and SST (middle panel) comparisons between (a, c) H9/AHI

1057 GEO satellite and (b, d) MODIS at 18:40 UTC on October 29, 2023. Comparisons of

1058 the one year (2023) (e) LST and (f) SST from MODIS and H9/AHI data over the

1059 NANO_SCS system. The color bar represents the total number in every bin at an

1060 interval of 0.25 K of LST or SST.

1061

1062

1063

1064
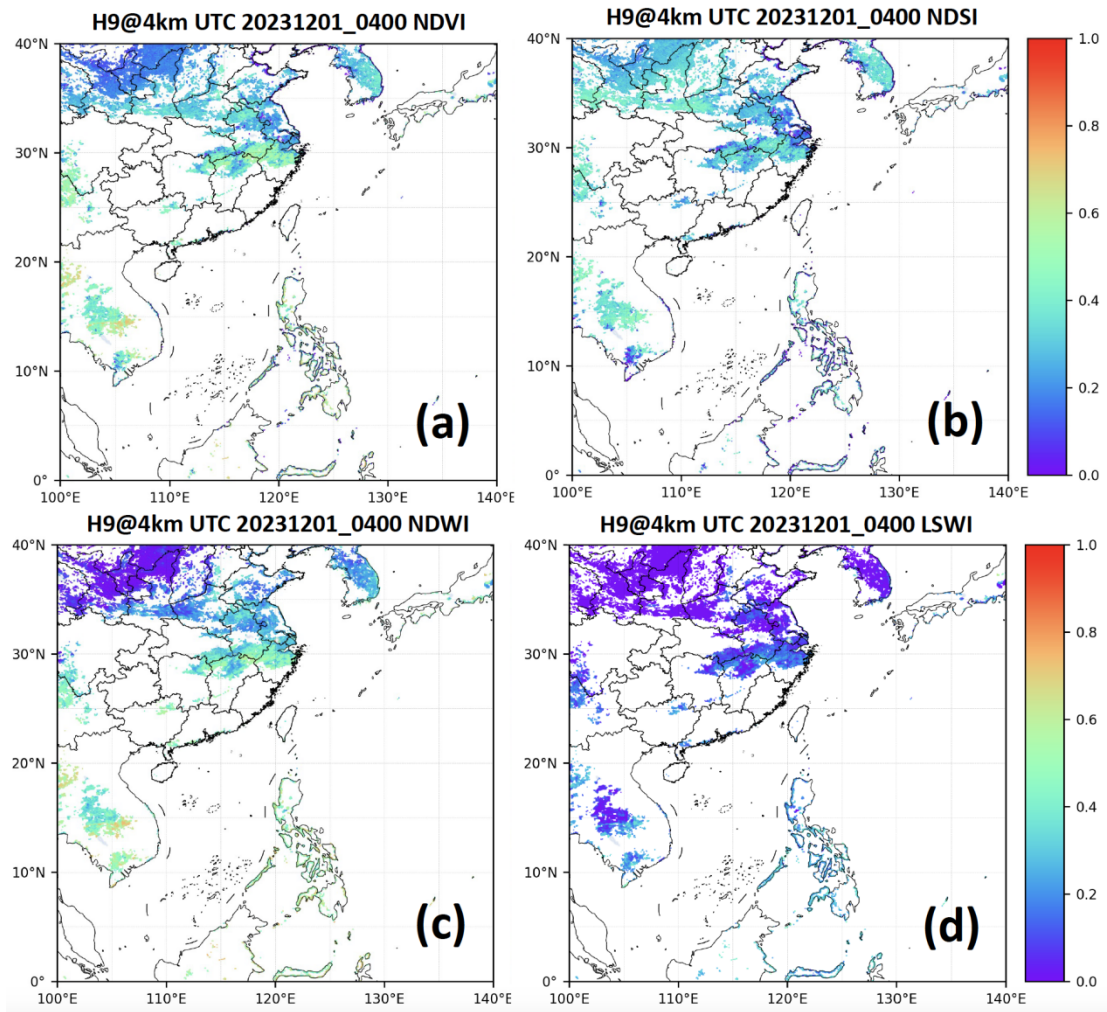
1065

Figure 10. (a) NDVI, (b) NDSI, (c) NDWI, and (d) LSWI maps retrieved by H9/AHI

at 04:00 UTC on December 1, 2023 over the NANO_SCS system.

1068